energies

MDPI

Article

Multi-Objective Capacity Configuration Optimization for Zero-Carbon Industrial Parks with CSP-Based Green Power Direct Connection

Bangjie Hu and Pei Wang *

School of Renewable Energy, Hohai University, Nanjing 211100, China; hubjsr@163.com
* Correspondence: wp198626@hhu.edu.cn

Abstract

Zero-carbon industrial parks (ZCIPs) must balance renewable supply, carbon emissions, and multi-energy reliability. This study examines capacity planning for a ZCIP connected to an external concentrated solar power (CSP) plant through a green power direct-connection contract. The contract gives the park bounded scheduling rights over its offtake and allows thermal energy storage (TES) charging or discharging within an agreed operating envelope; the CSP operator retains physical control of the plant. A tri-objective model minimizes annual cost, net accounted carbon emissions, and a representative-day supply adequacy deficit for electricity, heat, and cooling. Four seasonal typical days are used, and the problem is solved by an improved MOPSO. Under equal evaluation budgets, the improved algorithm achieves the highest mean HV and lowest mean IGD. CSP direct connection raises the hypervolume from 5.871×10^9 to 7.838×10^9; allowing electricity sales raises it from 4.563×10^9 to 8.508×10^9. Two stress cases, the maximum electricity-load day and maximum residual-load day, are evaluated using the fixed compromise configuration under a normal grid-connected boundary. The results support ZCIP planning and green power direct-connection policy design.

Keywords: zero-carbon industrial park; multi-objective optimization; carbon emission; supply reliability; capacity configuration; green electricity direct connection

1. Introduction

To achieve the dual-carbon goals of peaking carbon emissions by 2030 and achieving carbon neutrality by 2060, energy systems are accelerating the transition toward low-carbon and zero-carbon operation. Industrial parks, as the main carriers of industrial production and energy consumption, account for a considerable share of national energy consumption and CO_2 emissions, so zero-carbon industrial parks (ZCIPs) are regarded as a key pathway for balancing economic growth and emission reduction [1]. Nevertheless, the zero-carbon attribute cannot be realized simply by installing renewable energy: the inherent intermittency of wind and photovoltaic (PV) output forces the ZCIP to purchase electricity from the grid during periods of insufficient renewable generation, which inevitably leads to carbon emissions under the grid-average emission factor accounting [2].

To address this, green power direct connection policies have been introduced in China, allowing renewable plants to supply terminal users through dedicated lines or power purchase agreements, with the corresponding electricity treated as zero-carbon on the premise of green certificate issuance [3]. As a grid-friendly and dispatchable direct green

Check for updates

Academic Editor: Jarek Kurnitski

Received: 15 September 2026
Revised: 10 October 2026
Accepted: 11 October 2026
Published: 13 October 2026

Copyright: © 2026 by the authors. Licensee MDPI, Basel, Switzerland. This article is an open access article distributed under the terms and conditions of the Creative Commons Attribution (CC BY) license.

power source, a concentrated solar power (CSP) plant equipped with thermal energy storage (TES) can not only generate electricity but also transfer collected solar energy to the evening, thereby providing relatively stable green power across periods [4,5], and a real zero-carbon integrated energy system energized solely by CSP and PV has been demonstrated for an isolated grid [6]. This makes the scenario of "CSP green power direct connection + ZCIP" practically applicable, especially in northwest China where direct normal irradiance (DNI) is abundant and several CSP demonstration plants have been built. However, the configuration of the ZCIP, i.e., the capacity of self-built renewables, storage, and conversion equipment, is fundamental to its overall performance, since it determines the annualized investment cost, the annual carbon emissions, and the supply reliability of electricity, heat, and cooling. The capacity configuration of a ZCIP therefore needs to jointly consider economics, carbon emission, and supply reliability.

Capacity configuration is a core issue in the planning of integrated energy systems (IESs). Existing studies have developed double-layer optimization, heuristic algorithms, and typical-day methods to determine the capacities of renewable generators, storage, and conversion equipment, with objectives ranging from minimizing annual total cost to simultaneously balancing economic and environmental indicators. On the one hand, configurations are optimized toward low-carbon or zero-carbon operation: Chen et al. developed a near-zero-carbon building energy system integrating photovoltaics, cross-seasonal thermal storage, electrical storage, and heat pumps to address the mismatch between solar generation and building demand [7]; Xie et al. designed a fully green-electricity-supplied zero-carbon integrated energy station, modeling upstream renewable, generation, storage, transformer, and conversion capacities [8]; Wang et al. proposed a life-cycle-assessment-based robust multi-objective optimization model for a hybrid solar-assisted CCHP system driven by photovoltaic/thermal collectors and a gas turbine [9]; Han et al. proposed a multi-objective sustainability optimization model for a solar-based integrated energy system, using life-cycle energy analysis to describe resource inputs and pollutant emission costs [10]. On the other hand, configuration design is gradually extended toward economy, environment, and reliability: Shen et al. established a multi-objective capacity configuration model for an integrated energy system, minimizing annual cost and carbon emissions under cooling-driven-heat and heat-driven-electricity principles [11]; Li et al. proposed a life-cycle multi-objective capacity planning model for integrated energy systems under capacity tariffs, introducing an ecological damage index to balance economy, environment, and ecosystem [12]; Wang et al. developed a two-stage framework for planning photovoltaic installed capacity allocation, combining a multi-objective optimization model that minimizes supply–demand mismatch alongside economic and environmental profits with an entropy-weighted TOPSIS decision stage [13]; Yi et al. examined how carbon reduction targets influence the design and scheduling of a small-scale multi-source energy hub under solar uncertainty [14]. The integration of storage and heat supply is also considered, e.g., the series/parallel integration of latent heat storage in solar thermal systems [15], solar-assisted high-temperature heat pumps for off-grid zero-carbon heating in industrial parks [16], and next-generation zero-carbon heating plants combined with solar thermal/PV and thermal storage [17]. Methodologically, the capacity toolbox has been enriched by life-cycle multi-objective planning under cross-sectoral carbon emission flow [18], partitioned design for large-scale IESs [19], multi-parameter collaborative design for low-carbon park energy systems [20], and joint planning of reliability and low-carbon performance under multiple uncertainties [21]. Despite these advances, most of the reviewed capacity-planning studies focus on self-built wind, PV, and storage assets or treat CSP as an operational unit within the power plant. They rarely represent a CSP plant as an external, directly connected, and dispatchable green power source whose contracted supply

and TES-enabled temporal flexibility jointly influence ZCIP-side capacity decisions. Also, carbon emissions and multi-energy supply reliability are often simplified at the operational level or treated separately from capacity planning.

Once the equipment capacity is determined, the operation scheduling determines the actual output of each device, and low-carbon and economic scheduling of IESs has been widely studied from multiple perspectives. Carbon-constrained economic operation models that couple generation with carbon capture and storage and power-to-gas have been established for integrated energy systems [22,23], and power-carbon trading mechanisms combined with carbon emission cost criteria have been embedded into low-carbon operation models for park integrated energy systems [24]. Yin et al. proposed a hybrid multi-strategy improved beluga whale optimization algorithm for the economic operation of zero-carbon park multi-energy systems [25]; Zhao et al. developed an integrated energy system with concentrating solar power and multi-stage hydrogen utilization, optimized through ladder-type carbon trading for low-carbon economic scheduling [26]; Chen et al. optimized a residential building integrated energy system integrating a gas turbine, solar PV, heat pumps, electrical cooling, and storage, using multi-objective optimization and life-cycle assessment to evaluate energy savings, supply–demand matching, and exergo-environmental–economic indices under electric-following mode [27]. Dynamic programming and multi-layer scheduling frameworks have further supported low-carbon economic dispatch and the integration of power-to-X and carbon capture technologies [28,29]. To enhance flexibility and robustness, long-duration storage such as salt caverns has been integrated into electricity–hydrogen–carbon dispatch [30], distributed electricity–gas dispatch has been solved by variational inequalities and cooperative games [31], bi-level robust optimization has been adopted for resilient dispatch under renewable and demand fluctuations [32], master-slave games with integrated demand response have coordinated operator and user interests while balancing economic and environmental objectives [33], and energy hubs have been dispatched under bidirectional energy–carbon coupling with heterogeneous uncertainties [34]. However, these studies mainly improve operational dispatch performance after the equipment capacity is fixed; the feedback from carbon and supply-reliability requirements to capacity decisions therefore remains limited, which motivates a tighter coupling between capacity configuration and operation.

As carbon constraints are gradually incorporated into energy system planning, multi-objective optimization has become an important tool to balance multiple indicators such as economy and environment, and it is applied across both capacity configuration and operation scheduling. Non-dominated sorting genetic algorithms (NSGA-II/III) and multi-objective particle swarm optimization (MOPSO) are widely used in IESs, and decomposition-based algorithms such as the multi-objective evolutionary algorithm based on decomposition (MOEA/D) are also applied. Algorithmic improvements have been developed to strengthen convergence and Pareto-front quality, including improved genetic operators [35] and coevolutionary constrained multi-objective frameworks [36], while multi-objective heating-system optimization with a comprehensive economic–environmental-energy index has also been reported [37]. the technique for order preference by similarity to an ideal solution (TOPSIS), entropy weighting, and other decision methods are frequently combined with the resulting Pareto sets at different stages. Most existing multi-objective models consider two objectives, e.g., operating cost and carbon emission, or cost and exergo-environmental performance.

MOPSO is now widely used in multi-objective energy planning. Alkuhayli et al. used it in a three-objective energy management framework for multiple microgrids with coupled power and water constraints, balancing operating cost, pollution, and pump operation [38]. Li et al. combined NSGA-II and MOPSO for an electricity–gas–heat system

to reduce operating cost and increase wind and PV consumption [39]. For renewable and multi-energy system sizing, Cheraghi et al. applied MOPSO and NSGA-II to economic, technical, environmental, and social criteria for an autonomous building energy system [40], Chowdhury et al. compared MOPSO with GWO and TLBO for hybrid renewable energy system sizing [41], and Slama et al. compared NSGA-II and MOPSO for cost-reliability trade-offs in standalone hybrid systems [42]. MOPSO has also been applied to combined cooling, heating, and power systems. Soheyli et al. developed a co-constrained MOPSO for component sizing and penalty design, considering annual cost, system area, and loss-of-power/heat-supply probabilities [43]. Also, Lv et al. used MOPSO for thermodynamic, exergo–economic, and net-present-value optimization of a renewable cogeneration system [44]. These applications show that MOPSO can generate Pareto fronts for nonlinear, constrained energy problems, but performance depends on problem structure and metrics. It has shown fast convergence [41], while NSGA-II has produced broader or more uniform fronts in some cases [40,42], and hybrid NSGA-II-MOPSO schemes combine different search mechanisms [39]. Most reported MOPSO applications focus on microgrid management, renewable sizing, integrated dispatch, or plant-level CCHP. Few consider an external CSP plant whose contracted supply and TES flexibility shape ZCIP capacity decisions. Parameter reporting and fair comparisons among standard MOPSO, improved MOPSO, NSGA-III, and MOEA/D also remain limited. This study therefore does not claim MOPSO itself as the novelty; it focuses on integrating CSP direct-connection flexibility into ZCIP capacity planning and fairly evaluating an improved MOPSO for this problem. MOPSO and other multi-objective methods are well established, but their use for an external, directly connected CSP plant whose supply and TES flexibility affect ZCIP capacity decisions remains limited.

The literature provides a solid methodological base, but two gaps remain. First, capacity configuration and operation are often weakly connected: carbon emissions and multi-energy reliability are simplified at the dispatch stage or treated apart from planning. Second, CSP is usually studied as a plant-side asset or in isolated grids. Its role as an external, directly connected source whose contracted supply and TES flexibility affect ZCIP capacity choices has received little attention. These gaps motivate this study.

To address these gaps, this paper develops a tri-objective capacity configuration model for a ZCIP under CSP green power direct connection. The objectives are annual comprehensive cost, annual carbon emissions, and representative-day power–heat–cooling supply adequacy. Three contributions follow. First, unlike the planning studies [6–13] focused on self-built assets or plant-side CSP operation, this work treats CSP as an external, directly connected source. The contract gives the ZCIP bounded scheduling rights over the contracted electricity; the park can adjust offtake and request TES charging or discharging within contractual and technical limits, while the CSP operator remains responsible for physical dispatch, safety, and grid compliance. Second, an improved MOPSO with an external archive, crowding-distance-based leader selection, pbest updating, and mutation is developed and compared with standard MOPSO, NSGA-III, and MOEA/D. Third, scenario analysis examines how CSP direct connection and electricity selling affect capacity configuration and operation.

2. System Structure and Equipment Models

2.1. Equipment Composition and Modeling Boundary

The energy supply system of the ZCIP consists of two parts: the self-built power sources, storage, and energy conversion equipment of the ZCIP, and the external CSP power source and grid. The overall structure is shown in Figure 1. Considering that the

investment entities and operation modes of the various equipment differ, this paper first defines the construction boundary and modeling basis of the equipment.

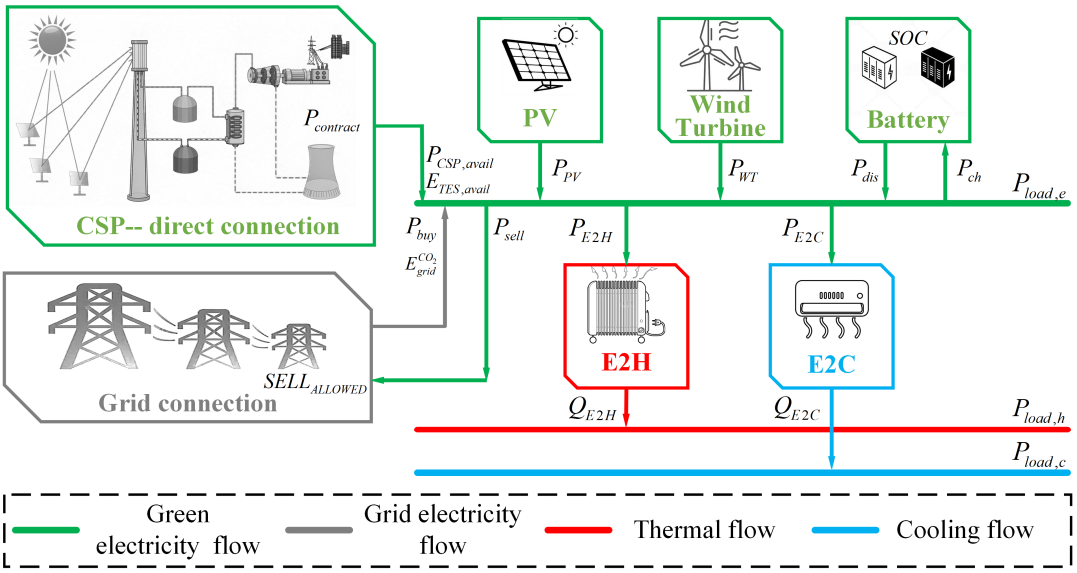


Figure 1. System structure of the ZCIP with CSP-based green power direct connection.

The self-built equipment in the ZCIP includes wind turbines, PV panels, battery energy storage, and electric heating and cooling devices. Electric heating is mainly provided by heat pumps or electric boilers, which convert electricity into the heat required by the ZCIP; electric cooling is mainly provided by electric chillers, and ice storage can be added when necessary to meet the cooling load. All of this equipment is invested in and built by the ZCIP, and its capacities (wind capacity, PV capacity, energy and power capacities of storage, electric heating capacity, and electric cooling capacity) are decision variables of the capacity configuration and are included in the annual investment cost. A single-node aggregated energy balance model is adopted inside the ZCIP, without considering the detailed topology of the distribution network, and hourly balance relations are established for the electricity, heat, and cooling flows.

The ZCIP does not build its own CSP plant. CSP plants with thermal energy storage have a large installed capacity, high unit investment, and large land occupation, and are usually built by power generation enterprises or large renewable energy bases as centralized power sources. Therefore, this paper does not include the CSP capacity as a decision variable in the ZCIP capacity configuration, but treats the CSP plant as an external green power source outside the ZCIP boundary. The ZCIP obtains CSP electricity through green power direct connection. The installed capacity and available output of the CSP plant are exogenous, whereas the contracted direct-connection capacity is a ZCIP-side planning variable defining the maximum power that can be delivered through the direct-connection line; the agreed electricity price and daily available electricity are also included in the model. The corresponding electricity is counted in the ZCIP carbon accounting at a zero-emission factor. To keep the model concise, this paper does not model the solar field, thermal storage, or turbine inside the CSP plant, but only retains its ability to shift green power output across periods, i.e., the ZCIP can flexibly schedule the timing of CSP green power consumption under contractual constraints.

Wind and PV power can be either self-built or obtained through green power direct connection. The self-built part is included in the decision variables of the ZCIP capacity configuration and the investment cost; the direct-connection part is represented by the contracted capacity and green power price, belongs to the external power supply of the

ZCIP, and is not included in the ZCIP investment cost. The self-built storage, electric heating, and electric cooling equipment of the ZCIP are all included in the investment cost.

The grid is treated as an available but finite external supply resource. Local generation consists of weather-dependent wind, PV, and CSP. Grid-constrained and islanded operation are outside this study.

In summary, the optimization objects of this paper include the self-built capacities of wind power, PV, storage, electric heating, and electric cooling, as well as the contracted direct-connection capacity. The CSP plant serves as an external green power source for direct connection; its installed capacity and available output are exogenously given, while the ZCIP determines the contracted direct-connection capacity and how to use the CSP green power. The two ways of obtaining wind and PV power, namely self-building and green power direct connection, correspond to different decision variables and cost bases.

No commercial CSP-to-ZCIP direct-connection project currently exists, so the arrangement is modeled as a prospective contractual flexibility service, not as a physical-control arrangement. The CSP operator controls the solar field, power block, and TES; the ZCIP only schedules contracted offtake and requests charging or discharging within a predefined operating envelope.

2.2. PV and Wind Power Output Models

PV power generation directly converts solar radiation into direct current through the photovoltaic effect, and its output power depends on the rated capacity of the PV array, the actual irradiance, and the cell temperature [45]. The PV output power can be expressed as

$$P_{PV}(t) = P_{PV}^{rate} \cdot \frac{I(t)}{I_{STC}}[1 + \beta_{PV}(T_{cell}(t) - T_{STC})] \tag{1}$$

where $P_{PV}(t)$ denotes the PV output power, MW; P_{PV}^{rate} denotes the rated capacity of the PV array, MW; $I(t)$ denotes the actual irradiance at time t, W/m^2; I_{STC} denotes the reference irradiance under standard test conditions, W/m^2, taken as 1000 in this paper; β_{PV} denotes the temperature coefficient of the PV output power, $-0.35/^{\circ}$C; $T_{cell}(t)$ denotes the PV cell temperature at time t, $^{\circ}$C; and T_{STC} denotes the reference temperature under standard test conditions, $^{\circ}$C, taken as 25.

A wind turbine first converts wind energy into mechanical energy and then into electrical energy through a generator, and its output power varies piecewise and nonlinearly with wind speed [30]. Considering the cut-in, rated, and cut-out wind speeds, the wind power output can be expressed as

$$P_{WT}(t) = P_{WT}^{rate} \cdot \begin{cases} 0, & v(t) \le v_{in} \text{ or } v(t) \ge v_{out} \\ \frac{v(t)^3 - v_{in}^3}{v_r^3 - v_{in}^3}, & v_{in} < v(t) \le v_r \\ 1, & v_r < v(t) < v_{out} \end{cases} \tag{2}$$

where $P_{WT}(t)$ denotes the wind power output, MW; P_{WT}^{rate} denotes the rated capacity of the wind turbine, MW; $v(t)$ denotes the wind speed at time t, m/s; v_{in} denotes the cut-in wind speed, m/s; v_r denotes the rated wind speed, m/s; and v_{out} denotes the cut-out wind speed, m/s.

2.3. Battery Energy Storage Model

Battery energy storage shifts electricity in time through charging and discharging. Its state of charge (SOC) varies with the charging and discharging power and is subject to the charging/discharging power limits, the SOC limits, and the initial and final state constraints.

The SOC recursion and limits, together with the initial and final state constraints, are given as follows:

$$\begin{cases} SOC(t+1) = SOC(t) + \left(\eta_{ch} P_{ch}(t) - \frac{P_{dis}(t)}{\eta_{dis}}\right) \frac{\Delta t}{E_{BESS}} \\ SOC_{min} \le SOC(t) \le SOC_{max} \\ SOC(1) = SOC_0 \\ SOC(T+1) = SOC_{end} \end{cases} \tag{3}$$

where $SOC(t)$ denotes the battery SOC at time t, p.u.; η_{ch} denotes the charging efficiency; η_{dis} denotes the discharging efficiency; $P_{ch}(t)$ denotes the charging power at time t, MW; $P_{dis}(t)$ denotes the discharging power at time t, MW; Δt denotes the dispatch time step, h; and E_{BESS} denotes the rated energy capacity of the storage, MWh; SOC_{min}, SOC_{max} denote the lower and upper limits of the SOC, p.u., respectively; SOC_0 denotes the initial SOC, p.u.; SOC_{end} denotes the SOC at the end of the dispatch period, p.u.; and T denotes the total number of dispatch periods.

The charging/discharging power limits and the mutual exclusion constraint are

$$\begin{cases} 0 \le P_{ch}(t) \le u_{ch}(t) P_{BESS} \\ 0 \le P_{dis}(t) \le u_{dis}(t) P_{BESS} \\ u_{ch}(t) + u_{dis}(t) \le 1 \end{cases} \tag{4}$$

where $u_{ch}(t)$ denotes the charging state variable at time t, 0/1; and $u_{dis}(t)$ denotes the discharging state variable at time t, 0/1; P_{BESS} denotes the maximum charging/discharging power of the storage, MW.

2.4. Electric Heating and Electric Cooling Models

Electric heating equipment converts electricity into heat through heat pumps or electric boilers, and its heat output and power consumption satisfy

$$\begin{cases} Q_{E2H}(t) = \eta_{E2H} P_{E2H}(t) \\ 0 \le Q_{E2H}(t) \le Q_{E2H}^{max} \end{cases} \tag{5}$$

where $Q_{E2H}(t)$ denotes the heat output of the electric heating equipment at time t, MW_{th}; $P_{E2H}(t)$ denotes the power consumption of the electric heating equipment at time t, MW; η_{E2H} denotes the conversion efficiency of the electric heating equipment; and Q_{E2H}^{max} denotes the rated heat output of the electric heating equipment, MW_{th}.

Electric cooling equipment converts electricity into cooling through electric chillers, and its cooling output and power consumption satisfy

$$\begin{cases} Q_{E2C}(t) = COP_{E2C} P_{E2C}(t) \\ 0 \le Q_{E2C}(t) \le Q_{E2C}^{max} \end{cases} \tag{6}$$

where $Q_{E2C}(t)$ denotes the cooling output of the electric cooling equipment at time t, MW_c; $P_{E2C}(t)$ denotes the power consumption of the electric cooling equipment at time t, MW; COP_{E2C} denotes the coefficient of performance of the electric cooling equipment; and Q_{E2C}^{max} denotes the rated cooling output of the electric cooling equipment, MW_c.

2.5. Grid Interaction and Carbon Intensity Model

The ZCIP interacts with the grid at the point of common coupling. The purchased and sold power are subject to the tie-line capacity and the mutual exclusion constraint, and electricity selling is controlled by the parameter $SELL_{ALLOWED}$ [46]. Electricity selling

is treated as a market transaction. The environmental attributes of exported renewable electricity transfer to the purchaser and are excluded from the ZCIP's carbon-offset balance.

$$\begin{cases} 0 \le P_{buy}(t) \le u_{buy}(t) P_{line} \\ 0 \le P_{sell}(t) \le u_{sell}(t) P_{line} \\ u_{buy}(t) + u_{sell}(t) \le 1 \\ u_{sell}(t) \le SELL_{ALLOWED} \end{cases} \tag{7}$$

where $P_{buy}(t)$ denotes the purchased power at time t, MW; $P_{sell}(t)$ denotes the sold power at time t, MW; $u_{buy}(t)$ denotes the electricity purchase state variable at time t, 0/1; $u_{sell}(t)$ denotes the electricity selling state variable at time t, 0/1; P_{line} denotes the tie-line capacity, MW; and $SELL_{ALLOWED}$ denotes the parameter indicating whether electricity selling is allowed, taking 1 to allow selling and 0 to prohibit selling.

The carbon accounting separates physical grid-related emissions from market-based offsets. Physical emissions are calculated from purchased electricity and dynamic grid emission factors. Eligible offsets include renewable electricity consumed inside the ZCIP and retired green certificates. The same green-electricity attribute cannot be counted twice. The net accounted carbon balance equals physical emissions minus these eligible offsets.

$$E_{phys}^{CO_2} = \sum_{t=1}^{T} EF_{grid}(t) P_{buy}(t) \Delta t \tag{8}$$

where $E_{phys}^{CO_2}$ denotes the annual physical carbon emissions from the electricity purchase of the ZCIP, tCO_2; $EF_{grid}(t)$ denotes the dynamic grid carbon intensity at time t, tCO_2/MWh; $P_{buy}(t)$ denotes the purchased power at time t, MW.

2.6. CSP Generation and Green Power Direct Connection Model

Under the contract, the ZCIP can adjust CSP offtake within the contracted capacity, daily energy limit, and agreed TES envelope. These adjustments are scheduling requests, not direct control of the CSP plant. The operator remains responsible for plant operation, TES safety, and grid dispatch compliance.

$$\begin{cases} 0 \le P_{green}(t) \le P_{contract} \\ \sum_{t=1}^{T} P_{green}(t) \Delta t \le E_{green}^{day} \end{cases} \tag{9}$$

where $P_{green}(t)$ denotes the CSP green power consumed by the ZCIP at time t, MW; $P_{contract}$ denotes the CSP green power direct-connection contract capacity, MW; and E_{green}^{day} denotes the daily available electricity of the CSP plant, MWh.

During periods when the grid has difficulty absorbing renewable energy (e.g., high wind and PV output and insufficient grid regulation capability), CSP green power is not allowed to be fed into the grid and can only be directly supplied to the ZCIP or stored. Therefore, an absorption-difficulty period indicator α(t) is introduced, where 1 indicates that CSP green power may be fed into the grid during that period and 0 indicates that it is not allowed. The power delivery and allocation satisfy the following constraints:

$$\begin{cases} P_{green}^{g2s}(s,t) \le \alpha(t) \cdot P_{g2s}^{max} \\ P_{green}(s,t) + P_{green}^{g2s}(s,t) + P_{green}^{curt}(s,t) = P_{green}^{avail}(s,t) + P_{green}^{adj}(s,t) \end{cases} \tag{10}$$

where $P_{green}^{g2s}(s,t)$ denotes the CSP green power fed into the grid at time t under scenario s, MW; $\alpha(t)$ denotes the indicator of the grid's renewable energy absorption difficulty

period, taking the value of 0 or 1; P_{g2s}^{max} denotes the maximum power allowed for the CSP green power to be fed into the grid, MW; $P_{green}^{adj}(s,t)$ denotes the net upward or downward adjustment of CSP electricity offtake relative to the baseline available power, enabled by TES charging and discharging at time t under scenario s, MW; $P_{green}^{curt}(s,t)$ denotes the CSP green power curtailment at time t under scenario s, MW; and $P_{green}^{avail}(s,t)$ denotes the available output power of the CSP plant at time t under scenario s, MW.

When α(t) = 0, the grid is in a period of difficulty in absorbing renewable energy. At this time, the CSP plant cannot deliver electricity to the grid, and CSP green power can only be directly supplied to the ZCIP, stored through thermal storage, or curtailed in extreme cases.

3. Multi-Objective Optimization Model

3.1. Decision Variables and Overall Framework

To reflect the annual operation characteristics of the ZCIP while ensuring computational efficiency, this paper uses the typical-day method to discretize the annual operation process: typical days in spring, summer, autumn, and winter are selected, each containing 24 time slots with a time resolution of 1 h [47]. The proportion of days represented by each typical day in the year is taken as the scenario weight W_s, and $\sum_s W_s = 1$ is satisfied. The annual operation indicators (such as annual electricity purchase, annual carbon emissions, and annual energy not supplied) can be obtained by weighted aggregation of the results of each typical day, i.e.,

$$\begin{cases} E_{annual} = 365 \cdot \sum_s W_s E_s \\ W_s = D_s / 365 \end{cases} \tag{11}$$

where D_s denotes the number of days represented by the s-th typical day in a year.

The four representative days serve as a computational surrogate for annual planning. The resulting reliability indicators are comparative planning metrics, not probabilistic annual adequacy estimates.

The installed capacity of the ZCIP is taken as the upper-level decision variable, including the self-built capacities of PV, wind power, storage, electric heating, and electric cooling, i.e.,

$$X = [P_{PV}, N_{WT}, P_{BESS}, Q_{E2H}, Q_{E2C}, P_{contract}]^T \tag{12}$$

where P_{PV} denotes the rated PV capacity, MW; N_{WT} denotes the number of wind turbines (rated capacity 3 MW), units; Q_{E2H} denotes the rated heat output of the electric heating equipment, MW_{th}; Q_{E2C} denotes the rated cooling output of the electric cooling equipment, MW_c; and $P_{contract}$ denotes the CSP green power direct-connection contract capacity, MW.

A conventional 2 h storage duration is adopted for the BESS. Accordingly, the rated charging/discharging power P_{BESS} is the only BESS capacity variable to be optimized, while the energy capacity is determined by multiplying this power by the storage duration, i.e., $E_{BESS} = 2P_{BESS}$.

The upper-level searches for schemes using MOPSO, and the lower level performs operation scheduling for each typical day/scenario. To unify the annualized basis, the capital recovery factor is introduced:

$$CRF = \frac{r(1+r)^n}{(1+r)^n - 1} \tag{13}$$

3.2. Upper-Level Multi-Objective Optimization Model

3.2.1. Optimization Objectives

The upper-level capacity optimization model of the ZCIP contains three objectives: annual comprehensive investment cost, annual carbon emissions, and annual power–heat–cooling supply adequacy deficit.

(1) Annual comprehensive investment cost. The annual comprehensive cost consists of the annualized investment cost and the annual operation and maintenance (O&M) cost:

$$\begin{aligned} &F_1 = CRF \cdot C_{INV}(x) + C_{OP}(x) \\ &\begin{cases} C_{INV} = c_{PV}P_{PV} + c_{WT}P_{WT} + c^P_{BESS}P_{BESS} + c^E_{BESS}E_{BESS} + c_{E2H}Q_{E2H} + c_{E2C}Q_{E2C} + c_{line}P_{contract} \\ C_{OP} = C_{OM} + C_{grid} + C_{CSP} + C_{carbon} + C_{shed} + C_{curt} + C_{policy} \end{cases} \end{aligned} \quad (14)$$

where F_1 denotes the annual comprehensive investment cost, 10^4 CNY; c_{PV}, c_{WT} denote the unit capacity investment costs of PV and wind power, 10^4 CNY/MW; c^P_{BESS}, c^E_{BESS} denote the unit power and unit energy investment costs of the storage, 10^4 CNY/MW and 10^4 CNY/MWh; c_{E2H}, c_{E2C} denote the unit capacity investment costs of electric heating and electric cooling, 10^4 CNY/MW; C_{OP} denotes the total annual operating cost of the ZCIP under capacity configuration x; C_{OM} denotes the annual O&M cost, 10^4 CNY; C_{grid} denotes the annual net cost of grid interaction, 10^4 CNY/MWh; C_{CSP} denotes the annual procurement cost of green electricity supplied through the CSP direct-connection contract, 10^4 CNY/MWh; C_{carbon} denotes the annual carbon emission trading cost, 10^4 CNY/tCO_2; C_{curt} represents the curtailment cost of wind, PV, and CSP output, 10^4 CNY/MWh; C_{shed} represents the load-shedding penalties for electricity, heat, and cooling, 10^4 CNY/MWh; and C_{policy} denotes the annual policy-compliance penalty incurred when the annual green power consumption or CSP direct-supply ratios fail to meet the prescribed policy thresholds, 10^4 CNY.

The C_{OP} comprises the annual equipment O&M cost, the net grid-interaction cost (grid electricity purchase cost minus electricity-sale revenue), the CSP direct-connection green power purchase cost, carbon emission trading cost, curtailment penalties for wind, PV, and CSP generation, load-shedding penalties for electricity, heat, and cooling, and policy-compliance penalties associated with green power consumption and CSP supply fulfillment. These components are evaluated at the optimal lower-level dispatch solution and are returned to the upper-level capacity-planning objective. All dispatch-dependent cost terms are calculated over the 24 h representative days and aggregated using their annual weights; the policy-compliance penalty is evaluated from the annual aggregated indicators returned by that model.

The annual O&M cost is calculated as a proportion of the investment cost:

$$C_{OM} = [c_{om,PV}P_{PV}(t) + c_{om,WT}P_{WT}(t) + c_{om,BESS}(P_{ch}(t) + P_{dis}(t)) + c_{om,E2H}Q_{E2H}(t) + c_{om,E2C}Q_{E2C}(t)]\Delta t \quad (15)$$

where $c_{om,PV}$, $c_{om,WT}$, $c_{om,BESS}$, $c_{om,E2H}$, $c_{om,E2C}$ denote the annual O&M cost of the equipment, %.

(2) Annual carbon emissions. The annual carbon emissions of the ZCIP mainly come from grid electricity purchase, while the wind, PV, and CSP green power direct-connection electricity is treated as zero-carbon and can be offset by green certificates. The annual carbon emissions calculated in this paper already include the green certificates generated by the self-built wind and PV power, which are used for the ZCIP's own offsetting and not for trading, and the remaining annual carbon emissions are offset annually by purchased tradable green certificates:

$$F_2 = 365 \cdot \sum_{s \in S} w_s \left(E^{CO_2}_{phys,s} - E^{CO_2}_{offset,s} \right)$$
$$\begin{cases} E^{CO_2}_{phys,s} = \sum\limits_{t \in T} EF_{grid}(t) P_{buy}(s,t) \Delta t \\ E^{CO_2}_{offset,s} = \sum\limits_{t \in T} EF_{grid}(t) \left[P_{green}(s,t) + P_{PV}(s,t) + P_{WT}(s,t) \right] \Delta t - EF_{avg} E_{cert} \end{cases} \quad (16)$$

where F_2 denotes the annual carbon emissions of the ZCIP, tCO_2; S denotes the set of typical days/scenarios; w_s denotes the annual weight (proportion of days) of the s-th scenario; E_{cert} denotes the amount of green-certificate electricity corresponding to retired certificates, MWh; EF_{avg} is the average grid emission factor in tCO_2/MWh; and $E^{CO_2}_{offset,s}$ denotes the total eligible carbon offset applied in the annual carbon-emission objective, expressed in tCO_2. It includes the emissions equivalent of renewable electricity consumed within the ZCIP and retired green certificates, with no double counting.

(3) Annual power–heat–cooling supply unreliability. The reliability-related objective is a representative-day supply adequacy deficit, not failure-based reliability. It measures the normalized electricity, heat, and cooling demand that cannot be supplied under four representative conditions with normal grid availability. It does not cover outage frequency, forced-outage probability, line failure, grid loss, N-1 contingency, or islanded adequacy. Lower values mean a smaller adequacy deficit and better supply adequacy under the modeled conditions. The unserved energy for power, heat, and cooling is obtained from the lower-level load-shedding variables.

$$\begin{cases} ENS_e = 365 \cdot \sum\limits_{s \in S} w_s \sum\limits_{t \in T} L_{shed,e}(s,t) \Delta t \\ ENS_h = 365 \cdot \sum\limits_{s \in S} w_s \sum\limits_{t \in T} L_{shed,h}(s,t) \Delta t \\ ENS_c = 365 \cdot \sum\limits_{s \in S} w_s \sum\limits_{t \in T} L_{shed,c}(s,t) \Delta t \end{cases} \quad (17)$$

where ENS_e denotes the annual energy not supplied for power, MWh; and $L_{shed,e}(s,t)$ denotes the power load shedding at time t under scenario s, MW; ENS_h denotes the annual energy not supplied for heat, MWh; $L_{shed,h}(s,t)$ denotes the heat load shedding at time t under scenario s, MW; ENS_c denotes the annual energy not supplied for cooling, MWh; and $L_{shed,c}$ denotes the cooling load shedding at time t under scenario s, MW.

EENS, EHNS, and ECNS denote representative-day unserved energy for electricity, heat, and cooling. They are not probabilistic expected values in this formulation.

The three unserved-energy components are normalized by their respective total loads and weighted to obtain the composite supply adequacy deficit.

$$F_3 = \alpha_e \cdot \frac{ENS_e}{E^e_{load}} + \alpha_h \cdot \frac{ENS_h}{E^h_{load}} + \alpha_c \cdot \frac{ENS_c}{E^c_{load}} \quad (18)$$

where F_3 is used as a compact indicator of the supply adequacy deficit, rather than as a probabilistic system reliability index; α_e, α_h, α_c denote the weights of the power, heat, and cooling supply adequacy deficits, respectively, taken as $\alpha_e = 0.5$, $\alpha_h = 0.35$, and $\alpha_c = 0.15$; and E^e_{load}, E^h_{load} E^c_{load} denote the annual total electricity, heat and cooling loads of the ZCIP, MWh. The weights are determined according to the relative importance of the three reliability dimensions in the ZCIP, with power–heat–cooling supply reliability assigned the highest weight, followed by heat and cooling supply reliability.

The annual electricity and heat load totals are calculated as

$$\begin{cases} E^{e}_{load} = 365 \cdot \sum\limits_{s \in S} w_s \sum\limits_{t \in T} P_{load,e}(s,t)\Delta t \\ E^{h}_{load} = 365 \cdot \sum\limits_{s \in S} w_s \sum\limits_{t \in T} P_{load,h}(s,t)\Delta t \\ E^{c}_{load} = 365 \cdot \sum\limits_{s \in S} w_s \sum\limits_{t \in T} P_{load,c}(s,t)\Delta t \end{cases} \tag{19}$$

where $P_{load,e}(s,t)$ denotes the electricity load at time t under scenario s, MW; $P_{load,h}$ and $P_{load,c}$ denotes the heat and cooling load at time t under scenario s, MW.

The indicators apply to the assumed normal grid-available boundary and are used to compare capacity configurations. They are not probabilistic full-year adequacy measures under grid failure or constrained import. The model excludes equipment outages, line faults, grid loss, protection failures, N-1 contingencies, and probabilistic event sequences. The indicator is therefore not a failure probability, SAIDI/SAIFI, LOLE, or full-year probabilistic adequacy measure.

3.2.2. Constraints of the Upper-Level Optimization Model

The self-built equipment capacities of the ZCIP are constrained by resources, land, and investment, and shall satisfy the lower and upper capacity limits:

$$\begin{cases} P^{min}_{PV} \le P_{PV} \le P^{max}_{PV} \\ P^{min}_{WT} \le P_{WT} \le P^{max}_{WT} \\ E^{min}_{BESS} \le E_{BESS} \le E^{max}_{BESS} \end{cases} \tag{20}$$

where $P^{min}_{PV}, P^{max}_{PV}$ denote the lower and upper limits of the PV capacity, MW; $P^{min}_{WT}, P^{max}_{WT}$ denote the lower and upper limits of the wind capacity, MW; and $E^{min}_{BESS}, E^{max}_{BESS}$ denote the lower and upper limits of the storage energy, MWh.

In the scenario of green power direct connection between the CSP plant and the ZCIP, in addition to the contract capacity, hourly available output, and daily available electricity constraints described above, the direct supply ratio of the CSP plant and the consumption ratio of the ZCIP's directly connected green power shall also be considered [1,3,48].

(1) Direct supply ratio constraint of the CSP plant. To ensure a stable direct supply relationship between the CSP plant and the ZCIP, the annual electricity directly supplied by the CSP plant to the ZCIP shall exceed 60% of its total annual generation. This constraint follows the minimum self-consumption requirement for green power direct connection in [3].

$$365 \cdot \sum_{s \in S} w_s \sum_{t \in T} P_{green}(s,t)\Delta t \ge 60\% \cdot E^{gen}_{CSP} \tag{21}$$

where $P_{green}(s,t)$ denotes the CSP green power consumed by the ZCIP at time t under scenario s, MW; w_s denotes the annual weight (proportion of days) of scenario s; Δt denotes the time step, h; and E^{gen}_{CSP} denotes the total annual generation of the CSP plant, MWh, obtained by converting the hourly available output and weights of the typical days.

(2) Green power direct-connection consumption constraint. The green power direct-connection electricity shall account for more than 30% of the total annual electricity consumption of the ZCIP. This threshold follows the minimum direct-connection share of total park electricity consumption specified in [1].

$$\sum_{s \in S} w_s \sum_{t \in T} P_{green}(s,t)\Delta t \ge 30\% \cdot \sum_{s \in S} w_s \sum_{t \in T} P_{load,e}(s,t)\Delta t \tag{22}$$

For the zero-carbon park, two additional green-electricity consumption thresholds from [1] apply: directly supplied green electricity must account for at least 50% of annual electricity consumption, and direct green electricity plus retired green certificates must account for at least 90%.

$$\begin{cases} \sum_{s\in S} w_s \sum_{t\in T} \left[P_{green}(s,t) + P_{PV}(s,t) + P_{WT}(s,t)\right]\Delta t \\ \quad \geq 50\% \cdot \sum_{s\in S} w_s \sum_{t\in T} [P_{load,e}(s,t) + P_{E2H}(s,t) + P_{E2C}(s,t)]\Delta t \\ \sum_{s\in S} w_s \sum_{t\in T} \left[P_{green}(s,t) + P_{PV}(s,t) + P_{WT}(s,t)\right]\Delta t + E_{cert} \\ \quad \geq 90\% \cdot \sum_{s\in S} w_s \sum_{t\in T} [P_{load,e}(s,t) + P_{E2H}(s,t) + P_{E2C}(s,t)]\Delta t \end{cases} \tag{23}$$

where $P_{green}(s,t)$ denotes the CSP green power consumed by the ZCIP at time t under scenario s, MW; $P_{load,e}(s,t)$ denotes the electricity load of the ZCIP at time t under scenario s, MW; $P_{PV}(s,t)$, $P_{WT}(s,t)$ denote the PV and wind power output at time t under scenario s, MW; $P_{E2H}(s,t)$, $P_{E2C}(s,t)$ denote the power consumption of electric heating and electric cooling, MW.

3.3. Lower-Level Operation Scheduling Model

3.3.1. Optimization Objectives

The lower-level performs operation scheduling for each typical day/scenario, with the objective of minimizing the sum of operation cost, carbon cost, and load-shedding penalty:

$$\begin{aligned} &\text{Min } f_{sch} = \sum_{t\in T} \left[C_{grid}(t) + C_{carbon}(t) + C_{green}(t) + C_{shed}(t) + C_{curt}(t)\right]\Delta t \\ &\begin{cases} C_{grid}(t) = c_{buy}(t)P_{buy}(s,t) - c_{sell}(t)P_{sell}(t) \\ C_{carbon}(t) = \lambda_C EF(t)\left[P_{buy}(t) - P_{PV}(t) - P_{WT}(t)\right] \\ C_{green}(t) = c_{green}(t)P_{green}(t) \\ C_{shed}(t) = \rho_e L_{shed,e}(t) + \rho_h L_{shed,h}(t) + \rho_c L_{shed,c}(t) \\ C_{curt}(t) = c_{curt}P_{curt}(t) \end{cases} \end{aligned} \tag{24}$$

where $c_{buy}(t)$ denotes the electricity purchase price at time t, CNY/MWh; $c_{sell}(t)$ denotes the electricity selling price at time t, CNY/MWh; λ_C denotes the carbon price, CNY/tCO_2; and ρ_e, ρ_h, ρ_c denote the penalty coefficients for power, heat, and cooling load shedding, CNY/MWh; c_{green} denote the CSP green power price, CNY/MWh; $P_{curt}(t)$ denotes the wind and PV curtailment power, MW; and c_{curt} denote the penalty coefficients for curtailment power.

3.3.2. Operation Constraints

In the optimization model, charging and discharging represent ZCIP-side requests permitted by the contract; they do not imply direct operation of the TES. The requests are bounded by contract capacity, daily energy, TES state-of-charge limits, charging/discharging power limits, and mutual exclusivity.

The electric power balance is

$$\begin{aligned} &P_{PV}(s,t) + P_{WT}(s,t) + P_{dis}(s,t) + P_{green}(s,t) + P_{buy}(s,t) + P_{shed,e}(s,t) \\ &= P_{load,e}(s,t) + P_{ch}(s,t) + P_{E2H}(s,t) + P_{E2C}(s,t) + P_{sell}(s,t) + P_{curt}(s,t) \end{aligned} \tag{25}$$

where $P_{dis}(s,t)$, $P_{ch}(s,t)$ denote the storage discharging and charging power, MW; $P_{green}(s,t)$ denotes the power supplied by the CSP green power direct connection, MW; and $P_{sell}(s,t)$ denotes the sold power, MW.

The heat power balance and cooling power balance are

$$\begin{cases} Q_{E2H}(s,t) + L_{shed,h}(s,t) = P_{load,h}(s,t) \\ Q_{E2C}(s,t) + L_{shed,c}(s,t) = P_{load,c}(s,t) \end{cases} \tag{26}$$

where $Q_{E2H}(s,t)$ denotes the heat output of the electric heating equipment, MW_{th}; $Q_{E2C}(s,t)$ denotes the cooling output of the electric cooling equipment, MW_c.

The unsupplied load shall not exceed the corresponding load:

$$\begin{cases} 0 \le L_{shed,e}(s,t) \le P_{load,e}(s,t) \\ 0 \le L_{shed,h}(s,t) \le P_{load,h}(s,t) \\ 0 \le L_{shed,c}(s,t) \le P_{load,c}(s,t) \end{cases} \tag{27}$$

where $L_{shed,e}(s,t)$ denotes the power load shedding, MW; and $L_{shed,h}(s,t)$ denotes the heat load shedding, MW.

To reflect the ZCIP's ability to regulate the CSP green power consumption, the operation constraints of green power direct connection must be further considered, including the consumption power adjustment, the electricity–heat conversion efficiency, and the thermal storage capacity dynamics, as detailed below.

(1) CSP green power consumption and thermal storage adjustment power. The ZCIP can request upward or downward adjustment of CSP offtake relative to the baseline. TES discharging provides upward adjustment, while charging provides downward adjustment within the contracted flexibility envelope.

$$\begin{cases} P_{green}^{adj}(s,t) = P_{dis,el}(s,t) - P_{ch,el}(s,t) \\ 0 \le P_{ch,el}(s,t) \le P_{ch,el}^{max} \cdot u_{CSP}(s,t) \\ 0 \le P_{dis,el}(s,t) \le P_{dis,el}^{max} \cdot (1 - u_{CSP}(s,t)) \end{cases} \tag{28}$$

where $P_{ch,el}(s,t)$ and $P_{dis,el}(s,t)$ are the electric powers corresponding to the charging and discharging of the thermal storage, respectively; $u_{CSP}(s,t)$ is a 0–1 state variable, taking 1 to indicate thermal storage charging in that period; $P_{ch,el}^{max}$ and $P_{dis,el}^{max}$ are the upper limits of the charging and discharging power, respectively. The remaining symbols are consistent with those above.

(2) Electricity–heat conversion efficiency. To account for the efficiency difference between the charging and discharging ends and to ensure the stability of the thermal storage feasible region, the maximum and minimum electricity–heat conversion efficiencies are used for charging and discharging, respectively, and the corresponding heat consumption rates are

$$\begin{cases} HR_{ch} = 1/\eta_{ch,max} \\ HR_{dis} = 1/\eta_{dis,min} \\ E_{ch}(t) = HR_{ch} \cdot P_{ch,el}(t) \cdot \Delta t \\ E_{dis}(t) = HR_{dis} \cdot P_{dis,el}(t) \cdot \Delta t \end{cases} \tag{29}$$

where $\eta_{ch,max}$ and $\eta_{dis,min}$ are the electricity–heat conversion efficiencies on the charging and discharging sides, respectively, taken as 0.431 and 0.306 in this paper; HR_{ch} and HR_{dis} are the corresponding heat consumption rates; and $E_{ch}(t)$ and $E_{dis}(t)$ are the stored and released heat, respectively.

(3) Thermal storage capacity constraint. To describe the real-time state of the CSP thermal storage after adjustment, a form of "baseline thermal storage curve + cumulative deviation" is adopted, satisfying

$$\begin{cases} dE(1) = (HR_{ch} \cdot P_{ch,el}(1) - HR_{dis} \cdot P_{dis,el}(1)) \cdot \Delta t \\ dE(t) = dE(t-1) + (HR_{ch} \cdot P_{ch,el}(t) - HR_{dis} \cdot P_{dis,el}(t)) \cdot \Delta t \\ E_{TES}(s,t) = E_{TES}^{avail}(s,t) + dE(t) \\ E_{TES}^{min} \le E_{TES}(s,t) \le E_{TES}^{max} \\ E_{TES}(s,N_T) = E_{TES}^{0} \end{cases} \tag{30}$$

where $dE(t)$ is the cumulative deviation relative to the baseline; $E_{TES}^{avail}(s,t)$ is the baseline thermal storage curve; E_{TES}^{min} and E_{TES}^{max} are the lower and upper limits of the thermal storage capacity, taken as $E_{TES}^{min} = 0.2\,E_{TES}^{max}$; E_{TES}^{0} is the initial stored heat, taken as $0.5\,E_{TES}^{max}$; and N_T is the total number of dispatch periods.

3.4. Solution Algorithm Based on Improved MOPSO

The capacity configuration problem of the ZCIP in this paper can be formulated as the following multi-objective optimization problem:

$$\begin{aligned} &\mathrm{Min} F(x) = [f_1(x), f_2(x), f_3(x)]^T \\ &s.t. g_i(x) \le 0, x \in \Omega \end{aligned} \tag{31}$$

where $F(x)$ denotes the objective function vector; f_1, f_2, f_3 denote the annual comprehensive cost, annual carbon emissions, and annual power–heat–cooling supply adequacy deficit, respectively; x denotes the upper-level decision variable vector; $g_i(x)$ denotes the i-th constraint; and Ω denotes the feasible region of the decision variables.

In MOPSO, the quality of a solution is evaluated by the Pareto dominance relation, which is defined as:

$$x_1 \prec x_2 \Leftrightarrow \forall k \in [1,2,3] : f_k(x_1) \le f_k(x_2) \wedge \exists j : f_j(x_1) < f_j(x_2) \tag{32}$$

where $x_1 \prec x_2$ denotes that solution x_1 dominates solution x_2.

The self-built equipment capacities of the ZCIP are encoded as the particle position, and each particle corresponds to a capacity configuration scheme:

$$X_i = [P_{PV}, N_{WT}, P_{BESS}, Q_{E2H}, Q_{E2C}, P_{contract}] \tag{33}$$

where X_i denotes the position vector of the i-th particle.

After the lower-level day-ahead scheduling model is invoked for each particle, the three objective values are calculated as the fitness of that particle.

The particle velocity and position are updated as follows, and the inertia weight decreases with iteration:

$$\begin{cases} v_i^{k+1} = w \cdot v_i^k + c_1 r_1 \left(pbest_i - x_i^k \right) + c_2 r_2 \left(gbest_i - x_i^k \right) \\ x_i^{k+1} = x_i^k + v_i^{k+1} \\ w = w_{max} - (w_{max} - w_{min}) \cdot \frac{k}{K_{max}} \end{cases} \tag{34}$$

where v_i^k, x_i^k denote the velocity and position of the i-th particle at the k-th generation; w denotes the inertia weight; c_1, c_2 denote the learning factor; r_1, r_2 denote a random number between [0, 1]; $pbest_i, gbest_i$ denote the personal best and global best positions; w_{max}, w_{min} denote the lower and upper limits of the inertia weight; and K_{max} denotes the maximum number of iterations.

To maintain the uniformity of the Pareto front, an external archive is used to store the current non-dominated solutions, and the crowding distance is used to maintain diversity:

$$d_i = \sum_{k=1}^{3} \frac{f_k(i+1) - f_k(i-1)}{f_k^{max} - f_k^{min}} \tag{35}$$

where d_i denotes the crowding distance of the i-th solution; $f_k(i+1), f_k(i-1)$ denote the values of the two adjacent solutions of the i-th solution on the k-th objective; and f_k^{max}, f_k^{min} denote the maximum and minimum values of the k-th objective.

To avoid premature aggregation of particles, the global best is selected from the archive by a crowding-distance-based binary tournament, and mutation is applied to selected dimensions:

$$x_{i,j} = x_{i,j} + \mathcal{N}(0, \sigma_j), if\ rand < p_m \tag{36}$$

where $\mathcal{N}(0, \sigma_j)$ denotes a normally distributed random variable with mean 0 and standard deviation σ_j; p_m denotes the mutation probability; and σ_j denotes the mutation standard deviation of the j-th dimension.

Constraints are handled by the Deb constrained dominance rule: feasible solutions are better than infeasible ones, and infeasible solutions are compared by their degree of violation. The constraint violation is defined as

$$V(x) = \sum_i \max(0, g_i(x)) \tag{37}$$

where $V(x)$ denotes the constraint violation of solution x.

The solution flow of the improved MOPSO is shown in Figure 2. The main steps are (1) initialize the particle swarm, the external archive, and the algorithm parameters; (2) invoke the lower-level scheduling for each particle and calculate the three objective values; (3) update the personal best according to Pareto dominance and maintain the external archive; (4) select the global best from the archive by crowding-distance-based binary tournament leader selection; (5) update the velocity and position by Equation (34) and perform boundary repair; (6) apply mutation by Equation (36); and (7) re-evaluate and iterate until the termination condition is met, and output the Pareto front.

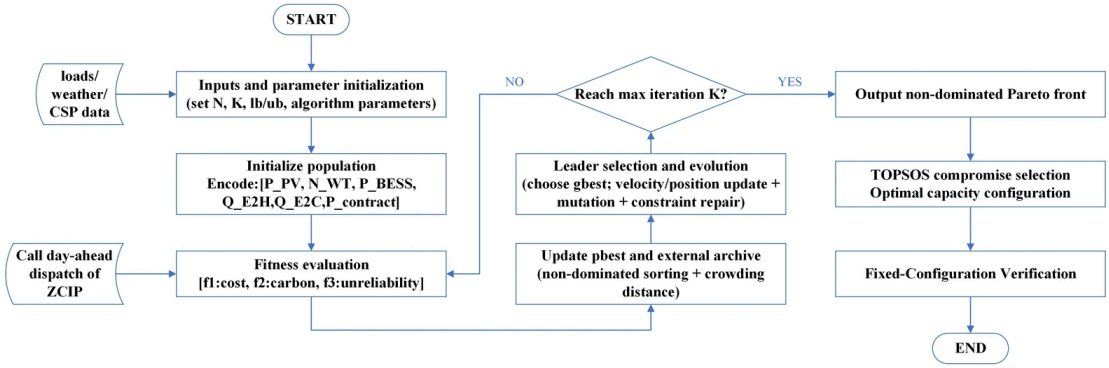


Figure 2. Flowchart of the improved MOPSO for the multi-objective configuration of the ZCIP.

4. Case Study

4.1. Basic Data and Parameters

The case study in this paper is based on a solar-resource-rich area in northwest China, where direct solar radiation is strong and the annual DNI is high, providing favorable conditions for building a CSP plant; a CSP plant with thermal storage has already been built there [49]. The local area is also promoting ZCIPs and green low-carbon demonstration

projects, with concentrated industries and concentrated electricity and heat demands, making it a suitable scenario for CSP green power direct connection. The full-year profiles of DNI, GHI, wind speed, and the electric, heating, and cooling loads are provided in Figures A1 and A2 of Appendix A. The detailed meteorological and load data are available in the Supplementary Material (provided as an .xlsx file).

Accordingly, the case scenario is set as follows: a CSP plant with thermal storage is deployed outside the ZCIP to supply contracted green power to the ZCIP through a green power direct-connection line; the ZCIP builds its own wind power, PV, storage, electric heating, and electric cooling equipment and interacts with the external grid, so as to examine the two cases of "electricity selling allowed" and "electricity purchase only". The zero-carbon goal of the ZCIP is achieved through self-built green power, CSP green power direct connection, and necessary green certificate offsetting, and the accounting boundary is net zero direct and indirect emissions within the operational scope.

The ZCIP adopts a single-node aggregated model, without considering the internal distribution network topology, and establishes hourly balance relations for the electricity, heat, and cooling flows. The CSP plant is regarded as an external green power source outside the ZCIP boundary; its installed capacity is given externally and is not included in the decision variables of the capacity configuration, and the ZCIP is connected to the delivered green power only through the green power direct-connection contract capacity, the agreed electricity price, the hourly available output, and the daily available electricity. The self-built capacities of wind power, PV, storage, electric heating, and electric cooling in the ZCIP constitute the upper-level decision variables. The equipment investment parameters and economic parameters are shown in Table 1. The investment costs for wind power, PV, battery storage, electric cooling, electric heating, and transmission-line construction were selected within the ranges reported in recent industry reports and relevant studies [50,51]. Since CSP-based green power direct connection currently lacks operational project or demonstration data, its electricity price is assumed in this case study based on the generation cost of CSP plants. Electricity tariffs, carbon emission intensities, and other economic parameters were obtained from the time-of-use tariff policies of the case-study region, relevant publicly available sources, and industry average values [52]. The shortage-penalty coefficients are adopted as internalized reliability penalty assumptions.

Table 1. Equipment investment and economic parameters.

Equipment	Investment Cost	Economic Indicator	Value
PV	4000 CNY/kW	Electricity tariffs (valley/flat/peak)	0.33/0.44/0.50 CNY/kWh
Wind power	6000 CNY/kW	CSP green power price	0.60 CNY/kWh
Energy storage capacity	800 CNY/kWh	Carbon intensity (valley/flat/peak)	0.40/0.55/0.70 tCO_2/MWh
Electric heating	1500 CNY/kW	Carbon price	100 CNY/tCO_2
Electric cooling	1200 CNY/kW	Discount rate	7%
Tie line	130 CNY/kW	Power/heat/cooling shortage penalty	20 CNY/kWh

The model does not consider direct carbon emissions from industrial processes or links such as hydrogen and carbon capture for the time being. The electricity purchased by the ZCIP is accounted for using the dynamic grid carbon intensity, while the wind, PV, and CSP green power direct-connection electricity is treated as zero carbon and can be offset by green certificates, thereby achieving net zero within the accounting boundary.

The four seasonal typical days are selected at a 1 h resolution, and the scenario weight of each typical day is defined as the number of days represented by that season divided by 365; in this case study, the spring, summer, autumn, and winter typical days represent 91, 90, 92, and 92 days, respectively. The four seasonal typical days are used to reduce the

computational burden of the capacity-planning problem. Under this boundary, the grid is treated as a normally available firm external resource, while all local generation sources are weather-dependent wind, PV, and CSP. Therefore, the reliability objective is interpreted as a representative-day planning indicator rather than a probabilistic full-year adequacy estimate. Figure 3 gives the per-unit output curves of PV and wind power on typical days in the four seasons. The PV output shows a typical intraday distribution, being zero at night and reaching a peak at 12:00–13:00; it is highest in spring (about 0.75 p.u.), followed by summer (about 0.70 p.u.) and autumn (about 0.55 p.u.), and lowest in winter (about 0.42 p.u.), broadly consistent with the seasonal solar radiation intensity. The wind output is also concentrated during the day and small at night. The reason for the "present by day and absent at night" pattern of wind power is that the nighttime wind speed at this site is generally low (about 1–2 m/s), below the cut-in wind speed of the turbines (3 m/s), so the output is close to zero; as the wind speed rises during the day, the output increases accordingly. It should be noted that the figure shows the average hourly wind speed in each season, and random gusts have been smoothed, so the curves appear relatively regular. Overall, the wind and PV output periods at this site overlap considerably, and the energy supply at night and during the evening peak relies mainly on energy storage and CSP thermal storage.

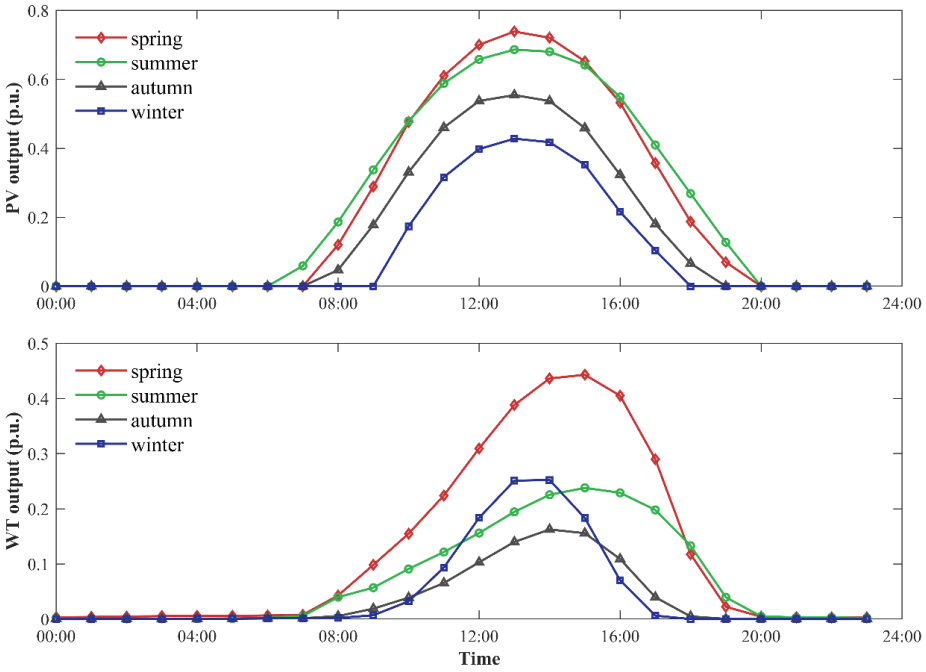


Figure 3. Per-unit output of PV and wind power on typical days in the four seasons.

Typical days are constructed from the daily average of the hourly load in each season to represent the operation scenarios of spring, summer, autumn, and winter, respectively, and the annual indicators are converted according to the number of days in each season. Figure 4 gives the electricity, heating, and cooling load distributions of the ZCIP on typical days in the four seasons. The loads show both seasonal and intraday variation. The electricity load is highest in winter, basically maintained at 80–90 MW, with an evening peak at 17:00–21:00; it is intermediate in spring and autumn, about 60–75 MW; in summer, a trough of about 50 MW occurs at 04:00–06:00. The heating load is largest in winter, with a heating peak at 06:00–12:00 of about 35 MW; it is next in spring and autumn; in summer there is almost no heating demand, and the load remains at a low level of about 15 MW. The seasonal pattern of the cooling load is opposite to that of the heating load, peaking in summer at 12:00–16:00 at about 20 MW and being lowest in winter. Because the

electricity and heating loads are both high in winter while the solar resource is weakest, this season is the most unfavorable scenario for power and heat supply reliability; the summer cooling load peak partly coincides with the PV output period. Therefore, the ZCIP capacity configuration needs to consider both the winter electricity–heating double peak and the summer cooling demand, and rely on thermal storage and battery storage for cross-period energy shifting.

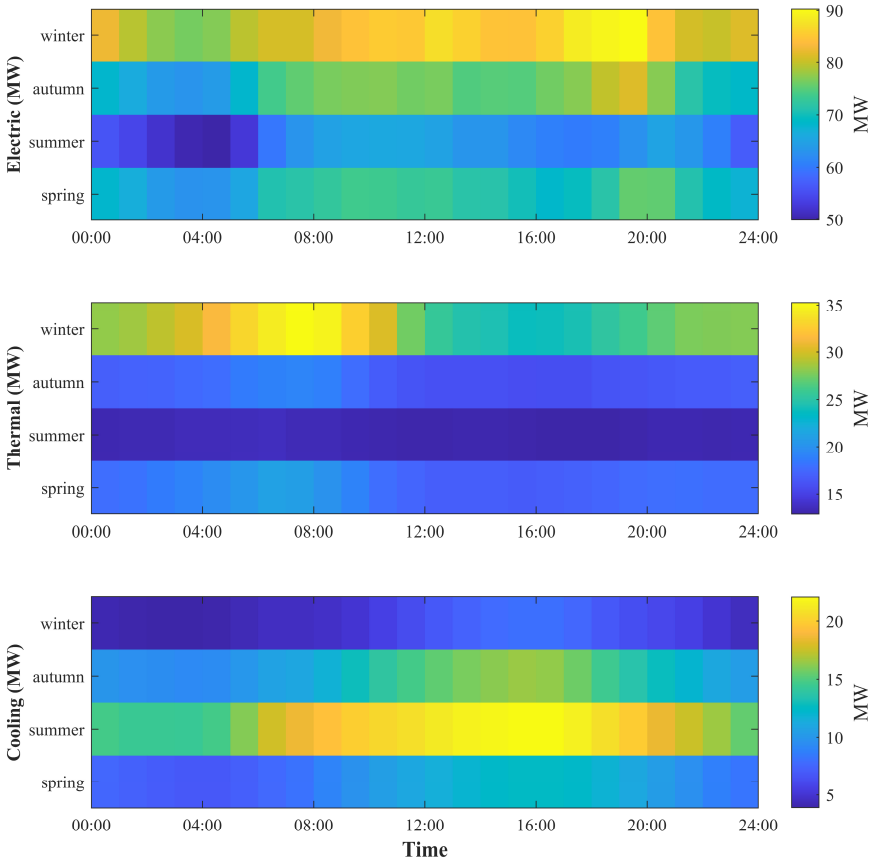


Figure 4. Electricity, heating, and cooling load distributions on typical days in the four seasons.

The lower and upper capacity bounds adopted for PV, wind power, BESS power, electric heating, electric cooling, and the CSP direct-connection contract capacity are set as follows: PV: 30–300 MW; wind power: 10–60 turbines × 3 MW/turbine; BESS: 10–100 MW; electric heating: 10–100 MW_{th}; electric cooling: 5–50 MW_c; and CSP direct-connection contract capacity: 30–120 MW.

The hourly available output of CSP green power direct connection is taken from the DNI data of a typical meteorological year, and the daily available electricity is jointly determined by the optimal operation strategy of the CSP plant itself and the configured thermal storage capacity [53,54]. Figure 5 gives the available generation power of the CSP plant (left axis, line) and the real-time capacity of the molten-salt thermal storage system (right axis, bars) on typical days in the four seasons. As a dispatchable renewable source with thermal storage, the available power of the CSP plant is not constant but shows a "low baseline + high peak" pattern. The thermal storage capacity always lies between the minimum stored heat (800 MWht, dashed line) and the rated thermal storage capacity (4000 MWht, solid line) on the typical days in the four seasons, following a "release at night/early morning and recharge in the afternoon" pattern. Across the four seasons, the thermal storage recharge is more complete in spring and summer (peak about 3000–3200 MWht) and relatively lower in autumn and winter (about 2500 MWht); the available power window in winter is more concentrated in the morning and evening.

Overall, the CSP plant has a peak-shaving capability, and its thermal storage system completes one charge–discharge cycle within a day and does not reach the rated capacity, indicating that the system still has some operating margin and can provide green power and thermal storage support for the ZCIP at night and during peak loads.

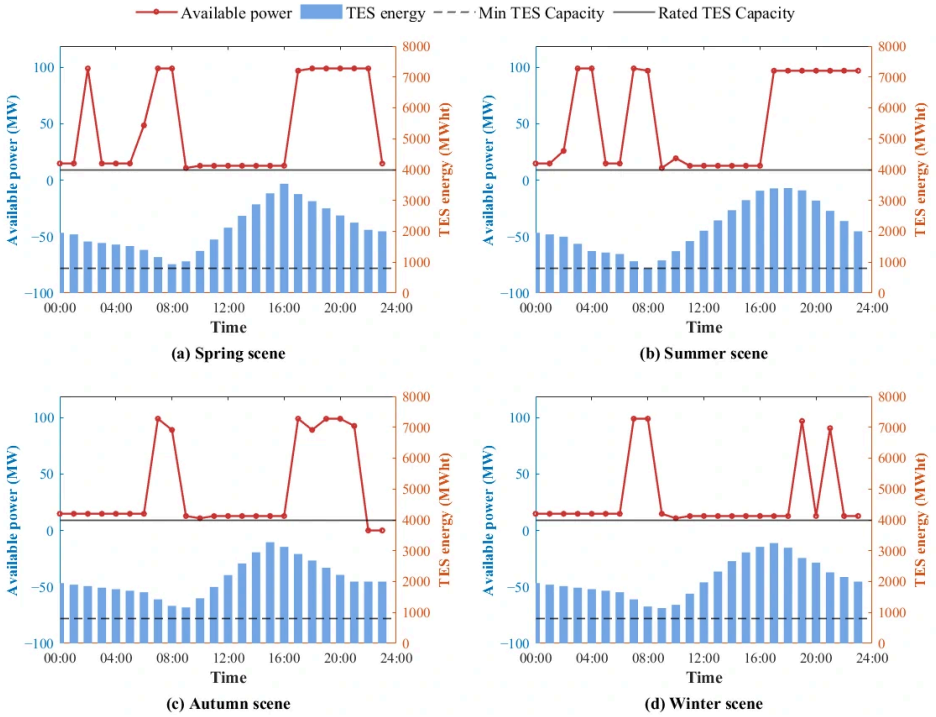


Figure 5. Available power and thermal storage capacity of the CSP plant on typical days in the four seasons.

4.2. Pareto Front and Compromise Solution of the Multi-Objective Optimization

4.2.1. Pareto Front

Figure 6 gives the Pareto front obtained by the improved MOPSO and its two-dimensional objective projections: (a) is the three-dimensional Pareto front of the annual comprehensive cost, net accounted carbon emissions, and annual power–heat–cooling supply adequacy deficit, and (b)–(d) are the two-dimensional projections of cost–carbon, carbon–supply adequacy deficit, and cost–supply adequacy deficit. The composite indicator denotes the representative-day supply adequacy deficit. The three-dimensional front shows clear mutual constraints among the three objectives, and the solution set forms a continuously distributed surface in the objective space, indicating that the algorithm obtained a non-dominated solution set with a wide coverage and relatively uniform distribution.

From the two-dimensional projections, cost and carbon emissions are clearly negatively correlated: as the annual comprehensive cost increases from about 2.5×10^7 CNY to 1.5×10^8 CNY, the net accounted carbon balance gradually decreases from about 200 tCO_2 to about -250 tCO_2, indicating that increasing the proportion of renewable energy, storage, and CSP direct connection can reduce net carbon emissions but requires a higher investment cost. Negative values represent accounting credits generated by renewable self-consumption and certificate retirement, not physical negative emissions. Cost and supply adequacy deficit are also negatively correlated: when the cost is low, the system supply adequacy deficit is about 1.2×10^{-3}, and when the cost increases, it can be reduced to about 6×10^{-4}, indicating that increasing the storage and dispatchable power capacity can improve the power–heat–cooling supply adequacy. Carbon emissions and the supply adequacy deficit are generally positively correlated, i.e., solutions with lower net accounted

carbon emissions usually have smaller supply adequacy deficits, reflecting a synergistic effect among green power consumption, storage configuration, and reliability.

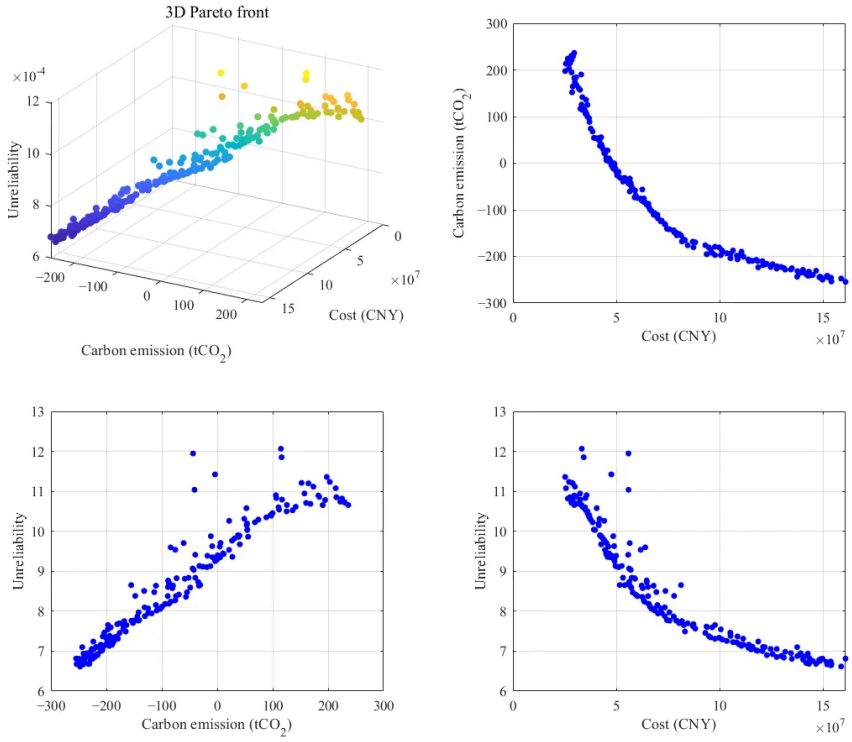


Figure 6. Pareto front and its two-dimensional objective projections.

It should be noted that the net carbon emissions of some solutions are negative, which is a result of the green-certificate offset accounting basis in this paper: when the self-built wind and PV power and the CSP green power of the ZCIP still have surplus after meeting their own loads (or are offset by green certificates and carbon credits), the net carbon emissions can be negative, i.e., a "net-negative-carbon/carbon-surplus" state. This Pareto front provides a complete trade-off solution set for the subsequent selection of the compromise solution, and decision makers with different preferences can select different capacity configuration schemes from it.

4.2.2. Compromise Solution

To select an engineering-usable representative configuration from the Pareto front, this paper uses TOPSIS (Technique for Order Preference by Similarity to an Ideal Solution) to determine the compromise solution. The procedure is as follows: first, the three objectives (annual comprehensive cost, annual carbon emissions, and annual power–heat–cooling supply adequacy deficit) are normalized, and the entropy weight method is used to determine the weight of each objective; then, the Euclidean distance from each solution to the ideal and negative-ideal solutions is calculated; finally, the solution with the largest relative closeness is taken as the compromise solution. This compromise solution balances the annual comprehensive cost, annual carbon emissions, and annual power–heat–cooling supply adequacy deficit and can serve as the recommended scheme for the capacity configuration of the ZCIP. The specific configuration is given in Table 2. The entropy weights of the annual comprehensive cost, annual carbon emissions, and annual power–heat–cooling supply adequacy deficit are $w = [w_1, w_2, w_3] = [0.451, 0.234, 0.315]$, respectively. The final decision set used for TOPSIS contains 200 non-dominated solutions, with closeness values ranging from 0.4652 to 0.7105; this set was obtained by merging the Pareto fronts from

multiple independent runs, re-sorting the combined solutions, and removing dominated or duplicate solutions.

Table 2. Capacity configuration and objective values of the compromise solution.

Item	Unit	Value
PV capacity	MW	204.61
Wind power capacity	MW	30.00
Storage power	MW	45.50
Storage energy capacity	MWh	91.00
Electric heating capacity	MW_{th}	30.22
Electric cooling capacity	MW_c	34.62
CSP green power direct-connection contract capacity	MW	99.73
Annual comprehensive cost	CNY/year	8.320×10^7
Net accounted carbon emissions	tCO_2/year	−165.09
Annual power–heat–cooling supply adequacy deficit	—	0.00

Negative values indicate a net market-based accounting credit, not physical carbon removal. Green-certificate procurement costs are not included in the present accounting.

Figure 7 gives the power dispatch results of the compromise solution on typical days in spring, summer, autumn, and winter. The positive values represent the supply side, including PV, wind power, CSP green power direct connection, storage discharge, and grid electricity purchase; the negative values represent the load and consumption side, including the electricity load, storage charging, electric heating, and electric cooling. Power supply and demand are balanced in all four seasons, with no obvious power shortage. In spring and autumn, the PV and CSP output is relatively high; the PV output is large at noon, the CSP plant supplies the main green power in the morning and evening, the storage performs peak shaving through "charging at valley periods and discharging at peak periods", and the grid electricity purchase is mainly concentrated at night and during the morning and evening load peaks. In summer, the PV output is high and the cooling load increases appreciably, so the share of electric cooling consumption rises, the CSP output is relatively low, and the storage and grid electricity purchase jointly ensure the peak load. In winter, the electricity load is the highest overall, the PV output is low, and the share of grid electricity purchase increases markedly; the CSP plant provides considerable green power in the morning and evening, and electric heating carries the main heating load.

Figure 8 compares the baseline available output of the CSP plant with the actual power consumed by the ZCIP under the compromise solution. The actual offtake can be lower or higher than the baseline available output within the agreed contractual envelope: lower offtake corresponds to TES charging, whereas higher offtake corresponds to TES discharging. This reflects the ZCIP's contractual ability to shift CSP green power consumption across periods according to its load and storage state. The observed deviations from the baseline curve therefore represent coordinated contractual scheduling requests within the agreed envelope, while the CSP operator remains responsible for the physical operation of the plant and TES. They do not imply unilateral physical control of the CSP facility.

On the whole, the compromise solution achieves power supply–demand balance on typical days in all four seasons, and PV, wind power, CSP, storage, and grid electricity purchase form a complementary supply structure: the CSP green power direct connection provides dispatchable green power during the morning and evening peaks, the storage performs peak shaving, and the grid electricity purchase serves as a fallback. This configuration achieves a good balance among economy, carbon emissions, and power–heat–cooling supply reliability and can serve as the recommended scheme for the capacity configuration of the ZCIP.

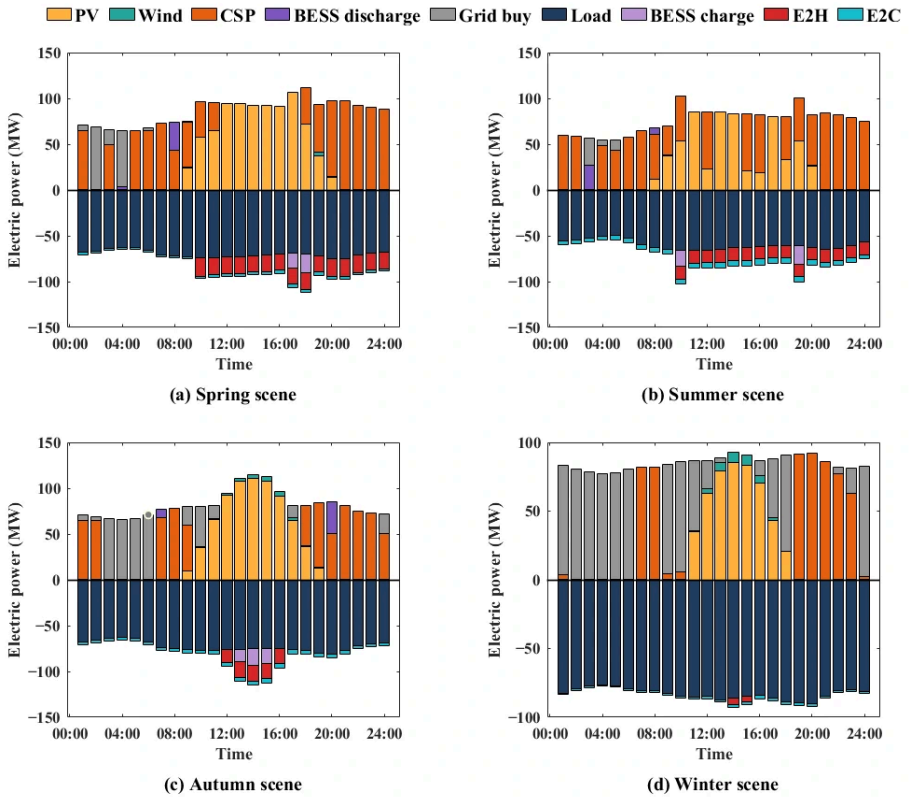


Figure 7. Dispatch results of the compromise solution on typical days in the four seasons.

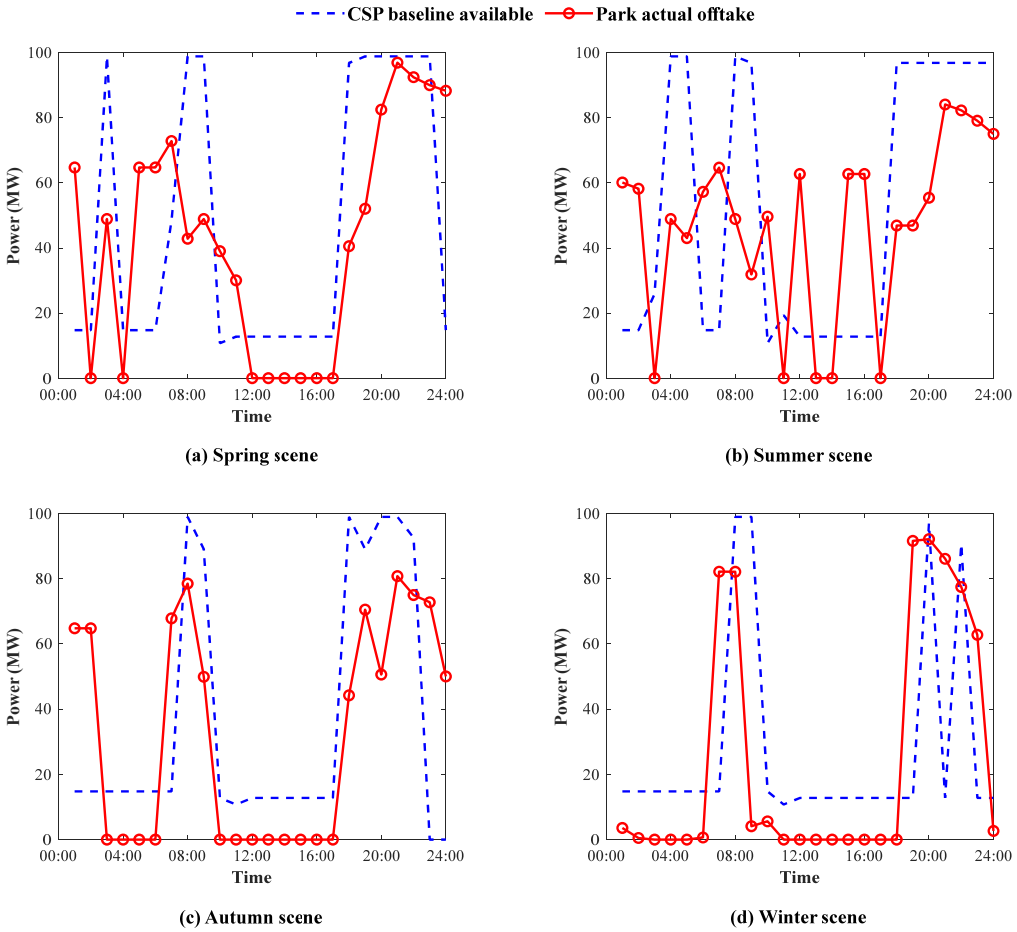


Figure 8. CSP plant dispatch curves of the compromise solution on typical days in the four seasons.

4.2.3. Fixed-Configuration Verification

This subsection is a deterministic stress check, not robust or stochastic optimization, and it does not assess probabilistic failure reliability. The compromise capacity configuration is fixed; only day-ahead dispatch is re-optimized. Two days are selected from the annual 8760 h dataset. The first is the annual maximum electricity-load day, which also coincides with the maximum combined electricity–heat load day and is similar to the maximum heat-load day. The second is the maximum residual-load day. Electricity, heat, and cooling loads are converted into an equivalent electricity demand; available PV, wind, and CSP output are subtracted; and the day with the largest positive residual load is selected. This identifies low renewable availability coinciding with high multi-energy demand. Grid import remains subject to the 80 MW tie-line limit in both cases. Severe grid-import restrictions, N-1 contingencies, and islanded operation are outside the present framework because they require reliability-constrained or robust optimization.

Figure 9a shows dispatch for the maximum electricity-load day. PV and CSP supply green power, BESS discharge covers part of the peak, and grid imports cover much of the remainder. Electric heating and cooling follow their loads, while BESS charging occurs mainly in lower-load periods. Supply and demand remain balanced, showing that the fixed configuration can meet the selected peak-load condition with grid support. This case checks peak-load supply capability, not outage reliability.

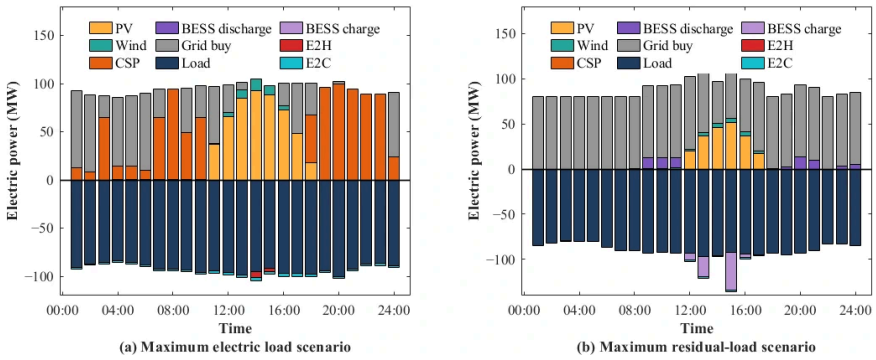


Figure 9. Power balance of the ZCIP under two scenarios.

Figure 9b shows dispatch for the maximum residual-load day. CSP available output and actual offtake are both zero. Demand remains high, so grid imports cover most of the load, PV contributes around midday, and BESS charging and discharging shift energy across periods. Electric heating and cooling follow their load requirements. The system remains balanced, showing that the fixed configuration can operate under this low-renewable/high-load condition. The case also shows greater dependence on grid imports and the role of BESS when CSP is unavailable. Since CSP available output and offtake are zero, the CSP/TES charging and discharging curves would also be zero, so no separate CSP dispatch figure is shown. This reflects the selected weather condition, not an omitted model component.

Figure 10 shows CSP plant and TES dispatch on the maximum electricity-load day. Actual CSP output follows the morning and evening peaks in available output and supplies relatively high green power during those periods. TES releases heat after the morning period and falls to about 800 MWh_t, close to its 20% lower limit. It then recovers at midday and discharges again in the evening. The TES therefore approaches but does not cross its lower limit and remains feasible. The two stress cases show that the fixed compromise solution remains feasible under normal grid-connected operation. The residual-load case also shows its reliance on grid imports and BESS regulation when CSP is unavailable.

These are deterministic stress checks, not probabilistic reliability, failure-event, N-1, or islanded-adequacy analyses.

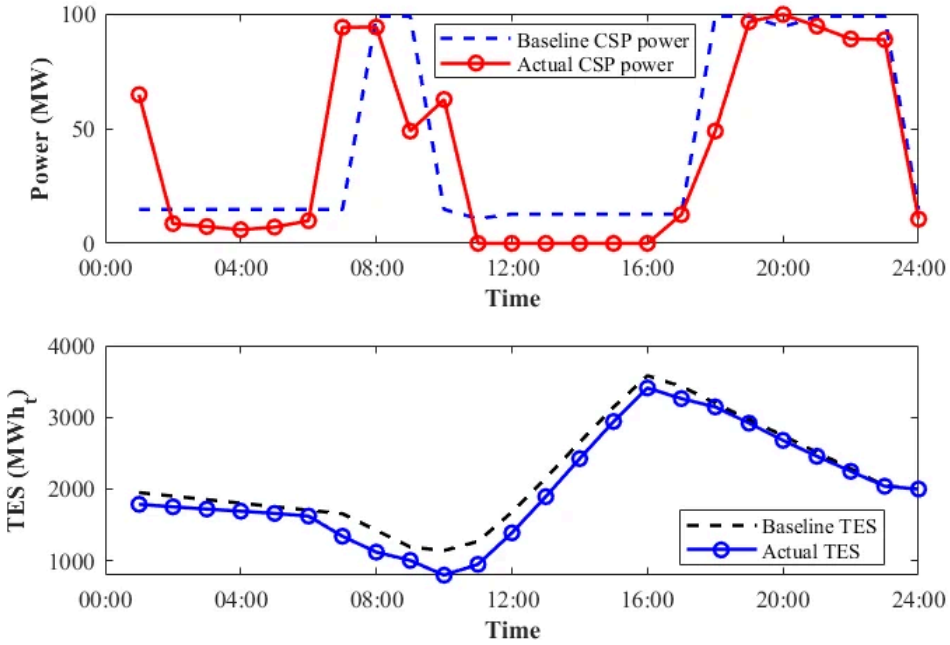


Figure 10. Dispatch curves of the CSP plant and TES system under the maximum electric load scenario.

4.3. Algorithm Performance Evaluation

4.3.1. Multi-Objective Performance Metrics

To objectively evaluate the convergence and distribution of the Pareto front obtained by the improved MOPSO, this paper uses three commonly used multi-objective performance metrics: hypervolume (HV), inverted generational distance (IGD), and spacing. A larger HV is better, and smaller IGD and spacing are better.

(1) Hypervolume (HV). It measures the volume of the objective space covered by the Pareto front and comprehensively reflects convergence and breadth. It is defined as

$$HV = \text{measure}\left(\underset{x \in PF}{\cup} \left\{ y \mid F(x) \prec y \prec y_{ref} \right\} \right) \tag{38}$$

where PF is the Pareto front obtained by the algorithm; F(x) is the objective vector of solution x; y_{ref} is the reference point, usually taken as the maximum value of each objective function or a point slightly larger than the maximum; and measure(·) denotes the Lebesgue measure, i.e., the hypervolume. A larger HV indicates that the front is closer to the ideal solution and covers a wider range.

(2) Inverted generational distance (IGD). It measures the average distance between the obtained front and the reference (true) front, reflecting convergence and distribution. It is defined as

$$IGD = \frac{1}{|PF^*|} \sum_{z \in PF^*} \min_{y \in PF} d(z, y) \tag{39}$$

where *PF** is the reference Pareto front, which is approximated in this paper by the non-dominated set obtained by merging multiple independent runs; PF is the Pareto front obtained by the algorithm; d(z,y) is the Euclidean distance between the reference point z and the front point y in the normalized objective space; and $|PF^*|$ is the number of reference front points. A smaller IGD is better.

(3) Spacing. It measures how uniformly the Pareto front solutions are distributed in the objective space. It is defined as

$$Spacing = \sqrt{\frac{1}{n-1}\sum_{i=1}^{n}(d_{avg} - d_i)^2} \quad (40)$$

where n is the number of Pareto front solutions, d_i is the distance between the i-th solution and its nearest neighbor in the objective space, and d_{avg} is the average of all d_i. A smaller spacing indicates a more uniform front distribution.

Because the three objectives differ greatly in dimension, the objective values are first normalized to the interval [0, 1] before calculating the above metrics, and a uniform reference point is set (e.g., 1.1 times the maximum value of each objective).

4.3.2. Comparative Analysis of Four Algorithms

To evaluate the performance of the improved MOPSO, it is compared with the standard MOPSO, NSGA-III, and MOEA/D under identical decision-variable bounds, the same lower-level scheduling model, and an equal objective-evaluation budget. The detailed parameter settings of the four algorithms are listed in Table 3. The algorithms use their standard or recommended operator settings, while the decision-variable bounds, lower-level scheduling model, evaluation budget, objective normalization, reference front, and HV reference point are identical. The common IGD reference front, denoted as PF^*, is constructed as the nondominated union of the final Pareto fronts obtained from all independent runs of the four algorithms. After objective normalization, the HV reference point is fixed at [1.1, 1.1, 1.1]. Gurobi 10.2 was used as the optimization solver, and all computations were performed in MATLAB R2023b on a computer equipped with an Intel Core i9-13900 processor.

Table 3. Parameter settings for the four comparison algorithms.

Algorithm	Improved MOPSO	Standard MOPSO	NSGA-III	MOEA/D
Population size	40	40	45	40
number of iterations	80	80	71	80
archive size	100	100	/	500
inertia and learning coefficients	$c_1 = c_2 = 2$	$c_1 = c_2 = 2$	/	/
mutation probability	0.01	/	1/6	1/6
MOEA/D neighborhood settings	/	/	/	20
NSGA-III reference directions	/	/	H = 8, M = 3	H = 8

Each algorithm is run independently multiple times, and the mean and standard deviation of HV, IGD, and spacing are recorded, as shown in Table 4.

Table 4. Comparison of multi-objective performance metrics of the four algorithms.

Algorithm	HV (Mean ± std)	IGD (Mean ± std)	Spacing (Mean ± std)	Total Runtime (s)
Improved MOPSO	0.9555 ± 0.0137	0.0366 ± 0.0023	0.0220 ± 0.0054	930.48
Standard MOPSO	0.7644 ± 0.0852	0.1560 ± 0.1123	0.0150 ± 0.0037	909.16
NSGA-III	0.2213 ± 0.0619	0.5219 ± 0.0951	0.0087 ± 0.0058	976.78
MOEA/D	0.1273 ± 0.0407	0.6017 ± 0.0532	0.0569 ± 0.0270	919.97

All algorithms use the same capacity limits, seasonal scenarios, weights, solver, and evaluation budget. NSGA-III and MOEA/D use standard settings, and standard

MOPSO serves as the baseline. The improved MOPSO adds an external archive with crowding-distance pruning, crowding-distance-based binary tournament leader selection, a dominance-based pbest update with 50% replacement for mutually nondominated solutions, and low-probability mutation that resets one randomly selected variable within its bounds. These changes aim to improve convergence and front distribution.

Figure 11 and Table 4 report the performance of the improved MOPSO, standard MOPSO, NSGA-III, and MOEA/D over 20 independent runs under identical decision-variable bounds and computational budgets. The improved MOPSO obtains the highest mean HV (0.9555 ± 0.0137) and the lowest mean IGD (0.0366 ± 0.0023), indicating better convergence and broader objective-space coverage than the other algorithms. Relative to the standard MOPSO, its mean HV is 25.0% higher, while its mean IGD is 76.5% lower; the relatively small standard deviations also indicate stable performance across the independent runs. NSGA-III obtains the smallest mean spacing (0.0087 ± 0.0058), indicating the most uniform distribution of solutions. However, its mean HV (0.2213 ± 0.0619) and mean IGD (0.5219 ± 0.0951) are less favorable than those of the improved MOPSO, indicating that its solutions are distributed more evenly but are farther from the reference front and cover a smaller portion of the objective space. The mean spacing of the improved MOPSO is 0.0220 ± 0.0054, which is larger than that of the standard MOPSO and NSGA-III but considerably smaller than that of MOEA/D. Overall, the improved MOPSO provides the most balanced performance among convergence, coverage, and distribution, and its comparatively low standard deviations indicate satisfactory repeatability for the tri-objective capacity-configuration problem. Because formal significance testing was not performed, these comparisons are interpreted descriptively rather than as evidence of statistical significance.

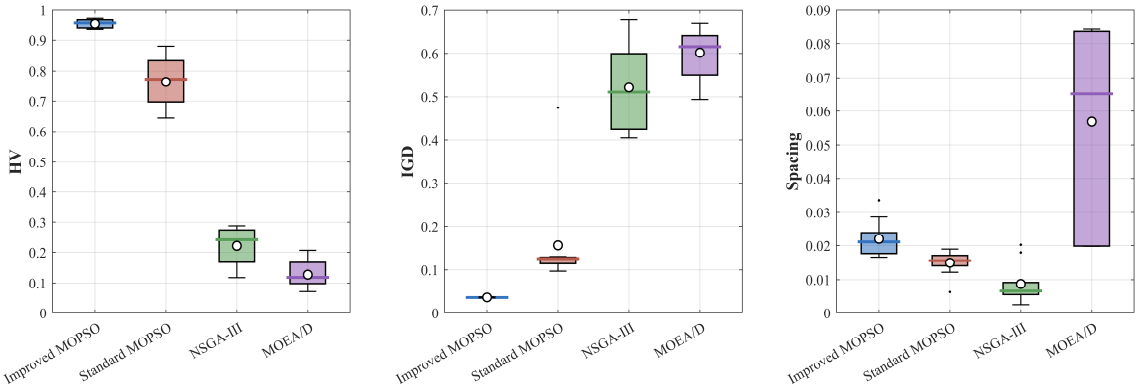


Figure 11. Comparison of multi-objective performance metrics.

Mean computation times for improved MOPSO, standard MOPSO, NSGA-III, and MOEA/D are 930.48, 909.16, 976.78, and 919.97 s. The four methods have comparable efficiency, with the largest difference about 7.5%. Standard MOPSO is fastest, followed closely by MOEA/D. Improved MOPSO is 2.3% slower than standard MOPSO and 1.1% slower than MOEA/D. NSGA-III is slowest, about 5.0% slower than improved MOPSO and 7.4% slower than standard MOPSO. Reported times are averages from the earlier repeated runs because device heating gradually increases runtime. Overall, improved MOPSO's runtime is comparable to standard MOPSO and MOEA/D and faster than NSGA-III, which is acceptable given its better HV and IGD.

4.4. Sensitivity Analysis

To examine the impact of key policies on the capacity configuration and operation performance of the ZCIP, this section conducts a sensitivity analysis on two factors: the CSP

green power direct connection and the electricity-selling interaction between the ZCIP and the grid. For each factor, comparative scenarios are set up and the annual multi-objective configuration optimization is re-performed. To reflect the impact of parameter changes, this paper compares the overall shape and quality of the two Pareto fronts, calculates the HV of each scenario front using the same reference point, and calculates the set coverage C(A,B)/C(B,A) between the scenario fronts. Scenario A is the baseline scenario: the CSP green power direct connection is considered, and the ZCIP only purchases electricity from the grid and does not sell electricity to the grid.

4.4.1. Impact of CSP Green Power Direct Connection

To analyze the impact of the CSP green power direct connection on the ZCIP configuration, two comparative scenarios are set up: Scenario A includes the CSP green power direct connection (baseline scenario), in which the ZCIP obtains CSP power through green power direct connection; Scenario B does not include the CSP green power direct connection, in which the ZCIP relies only on self-built wind power, PV, storage, and grid electricity purchase to meet the load. Both scenarios are re-optimized for multi-objective configuration based on the typical days in the four seasons of the year, and their respective Pareto fronts are obtained. For an objective comparison, this paper does not use a single compromise solution as the basis, but instead calculates the HV of the two scenario fronts using the same reference point and calculates the set coverage C(A,B) and C(B,A) between the scenario fronts; meanwhile, the two fronts are overlaid in 3D and pairwise objective projections to reflect the shift of the CSP direct connection on the feasible region and overall performance. In the scenario without green power direct connection, the compromise solution is for reference only, and the specific configuration is PV 176.77 MW, wind power 30 MW, storage power 42.93 MW, storage capacity 85.86 MWh, electric heating power 25.21 MW, and electric cooling 18.98 MW.

Table 5 gives the quality metrics of the Pareto fronts under the two scenarios with and without the CSP green power direct connection. The hypervolume of the scenario with the CSP green power direct connection is 7.838×10^9, higher under this comparison than 5.871×10^9 of the scenario without the CSP direct connection; the set coverage of the front with the CSP direct connection over the solutions of the scenario without the CSP direct connection is C(A,B) = 1.000, while the coverage of the scenario without the CSP direct connection over the solutions of the scenario with the CSP direct connection is C(B,A) = 0.000. It can be seen that the Pareto front of the scenario with the CSP green power direct connection is overall better in the objective space and dominates all non-dominated solutions of the latter.

Table 5. Quality metrics (HV, C(A,B), C(B,A)) of the Pareto fronts under different CSP direct-connection scenarios.

Scenario	HV	C(A,B)	C(B,A)
CSP plant green power direct connection	7.838×10^9	1.000	\
Without green power direct connection	5.871×10^9	\	0.000

Figure 12 further gives the overlay comparison of the Pareto fronts of the two scenarios. At the same annual comprehensive cost level, the scenario with the CSP green power direct connection (blue) has lower annual carbon emissions and lower annual power–heat–cooling supply adequacy deficit, and its front is overall located in the lower-left region of the scenario without the CSP direct connection (red); the front of the scenario without the CSP direct connection shifts overall to the upper right, i.e., a higher cost is required to achieve the same carbon emissions and supply adequacy level. This indicates that the

CSP plant, as a dispatchable green power source participating in the green power direct connection of the ZCIP, can not only reduce the net carbon emissions of the ZCIP but also provide stable green power during the morning and evening peaks and improve the power–heat–cooling supply reliability, without a substantial increase in the system cost. Therefore, introducing the CSP green power direct connection helps improve the overall performance of the ZCIP.

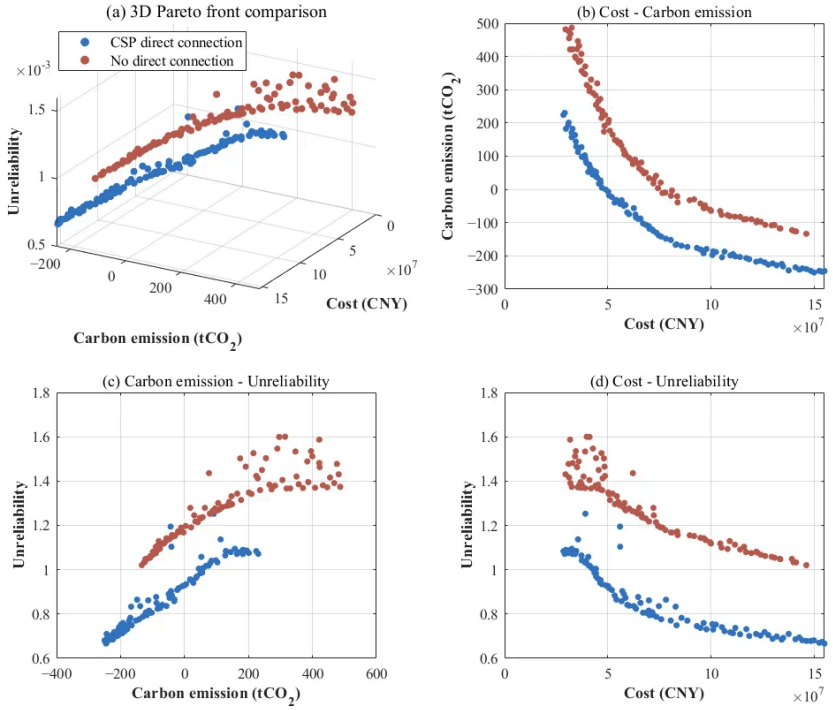


Figure 12. Comparison of Pareto fronts under different CSP direct-connection scenarios.

The above results show that the scenario with the CSP green power direct connection (A) has a higher hypervolume at the same reference point, and its Pareto front has a higher dominance coverage over the solutions of the scenario without the CSP (B), indicating that introducing the CSP green power direct connection improves the overall performance of the configuration scheme; the fronts of the two scenarios shift in the cost–reliability direction, and the CSP direct connection achieves better carbon emissions and reliability at a very small cost increase.

4.4.2. Impact of Grid Interaction and Electricity Selling

To analyze the impact of the electricity-selling interaction between the ZCIP and the grid, Scenario C is set up to allow the ZCIP to sell electricity to the grid (*SELL_ALLOWED* = 1, surplus electricity may be fed into the grid). The two scenarios are also re-optimized for multi-objective configuration based on the typical days in the four seasons of the year. The comparison method is the same as above: the hypervolume of the two scenario fronts is calculated using the same reference point, the set coverage C(A,C) and C(C,A) is calculated, and the two Pareto fronts are overlaid to illustrate the impact of the electricity-selling mode on the feasible region and overall performance. In the scenario without the green power direct connection, the compromise solution is for reference only, and the specific configuration is PV 200 MW, wind power 30 MW, storage power 26.21 MW, storage capacity 52.42 MWh, electric heating power 20.58 MW, electric cooling 25.80 MW, and CSP green power direct-connection contract capacity 62.24 MW.

Table 6 gives the quality metrics of the Pareto fronts under the two scenarios of electricity purchase only and both electricity purchase and selling. The hypervolume of the

electricity-selling scenario is 8.508×10^9, higher under this comparison than 4.563×10^9 of the electricity-purchase-only scenario; the set coverage between the two scenario fronts is C(A,C) = 0.040 and C(C,A) = 0.040, respectively, indicating that each scenario has a small number of solutions that dominate the other, but the electricity-selling scenario covers a larger objective space and has a higher front quality.

Table 6. Quality metrics of the Pareto fronts under different electricity-selling scenarios.

Scenario	HV	C(A,C)	C(C,A)
Electricity purchase only, no selling	4.563×10^9	0.040	\
Electricity purchase and selling	8.508×10^9	\	0.040

Figure 13 gives the overlay comparison of the Pareto fronts of the two scenarios. The front of the electricity-selling scenario (red) can extend to a lower net carbon emission region in the cost–carbon plane, i.e., by feeding surplus green power into the grid, the ZCIP obtains a larger carbon reduction space; the electricity-purchase-only scenario (blue) has more solutions in the lower-cost region, but its lower bound of net carbon emissions is clearly higher than that of the electricity-selling scenario. At the same time, the unreliability distribution range of the electricity-selling scenario is slightly wider, indicating that electricity selling, while improving the green power consumption and carbon reduction capability, may also bring additional trade-offs in the operation strategy. Overall, the electricity-selling scenario expands the low-carbon feasible region by allowing surplus renewable electricity to participate in market-based transactions. Because the selling scenario assumes market-based export and the transfer of environmental attributes to the purchaser, it does not imply an unconditional right to export. In addition, the 20% export limit and certificate-procurement cost are not modeled, so the result is a market-enabled sensitivity analysis rather than a direct assessment of statutory policy compliance; these assumptions are stated as limitations [3].

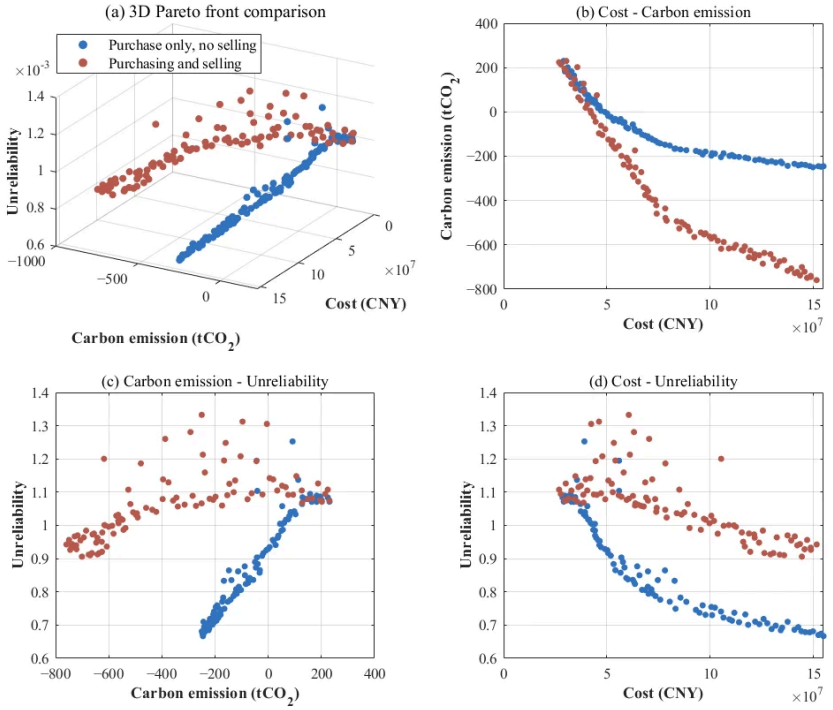


Figure 13. Comparison of Pareto fronts under different electricity-selling scenarios.

5. Conclusions

This paper develops a tri-objective capacity configuration model for a ZCIP with CSP green power direct connection. The CSP operator retains physical control of the plant and TES; the ZCIP schedules contracted offtake and requests TES charging or discharging within the contractual envelope. The objectives are annual comprehensive cost, net accounted carbon emissions, and a representative-day power–heat–cooling supply adequacy indicator. Two deterministic stress cases, the maximum electricity-load day and the maximum residual-load day, verify the fixed compromise configuration under normal grid-connected operation. The Pareto front is continuous and wide, with clear trade-offs. More renewable, storage, and contracted CSP capacity lowers the net accounted carbon balance and supply adequacy deficit but increases annual cost. The compromise solution balances the three objectives under the modeled boundary.

The CSP direct connection improves ZCIP performance. Hypervolume rises from 5.871×10^9 to 7.838×10^9, and the direct-connection front dominates all nondominated solutions of the no-direct-connection case. At similar cost, the direct-connection scenario has a lower net accounted carbon balance and lower power–heat–cooling supply adequacy deficit. These gains come from contracted scheduling flexibility and TES operation, not direct physical control of the CSP facility.

Electricity sale expands the low-carbon feasible region: hypervolume rises from 4.563×10^9 to 8.508×10^9, and the front extends to a lower net accounted carbon balance. This result is a market-enabled sensitivity case because the 20% export limit and certificate-procurement cost are not modeled. In the algorithm comparison, improved MOPSO has the highest mean HV (0.9555 ± 0.0137) and lowest mean IGD (0.0366 ± 0.0023); NSGA-III has the best spacing (0.0087 ± 0.0058). The four algorithms have comparable runtime. Reliability is interpreted as a representative-day supply adequacy deficit under normal grid availability, not failure-based reliability. The two stress cases show that the peak-load day remains balanced with CSP/TES and grid support, while the maximum residual-load day has zero CSP output and relies mainly on grid imports, PV, and BESS. They define an operating boundary and grid dependence, not robust optimization, failure probability, N-1 contingency, or islanded adequacy.

Future work will include full-year stochastic adequacy, constrained-grid and islanded operation, contractual allocation of CSP dispatch rights and TES flexibility, explicit green-certificate transactions and purchase costs, and implementation of the 20% export limit in the applicable direct-connection policy.

Supplementary Materials: The following supporting information can be downloaded at: https://www.mdpi.com/article/10.3390/en19204834/s1, Data.xlsx: Detailed meteorological and load data.

Author Contributions: B.H.: writing—original draft, software, methodology, visualization. P.W.: writing—review and editing, supervision, project administration. All authors have read and agreed to the published version of the manuscript.

Funding: This research was supported by Key project of the National Natural Science Foundation of China [grant number U2243243].

Data Availability Statement: The annual load and meteorological time series used in this study are provided in Appendix A. Other supporting data are available from the corresponding author on reasonable request. Some CSP plant operating data and other parameters cannot be publicly released because they are subject to third-party commercial confidentiality; these data are reported only in aggregated or normalized form in this paper.

Conflicts of Interest: The authors declare no conflicts of interest.

Abbreviations

The following abbreviations are used in this manuscript:

ZCIP	Zero-carbon industrial park
CSP	Concentrated solar power
PV	Photovoltaic
TES	Thermal energy storage
IES	Integrated energy system
MOPSO	Multi-objective particle swarm optimization
NSGA-III	Non-dominated sorting genetic algorithm III
MOEA/D	Multi-objective evolutionary algorithm based on decomposition
TOPSIS	Technique for order preference by similarity to an ideal solution
HV	Hypervolume
IGD	Inverted generational distance
SOC	State of charge
DNI	Direct normal irradiance
O&M	Operation and maintenance

Appendix A

Figures A1 and A2 present the annual DNI, GHI, wind speed, and cooling, heating, and electric load data used in this study. The series are hourly over a full year. The heatmaps show day of year horizontally and hour of day vertically, so seasonal and intraday patterns are visible. Figure A1a–c show DNI, GHI, and wind speed; Figure A2a–c show electric, heating, and cooling loads in MW. These profiles define the boundary conditions for capacity configuration and day-ahead dispatch.

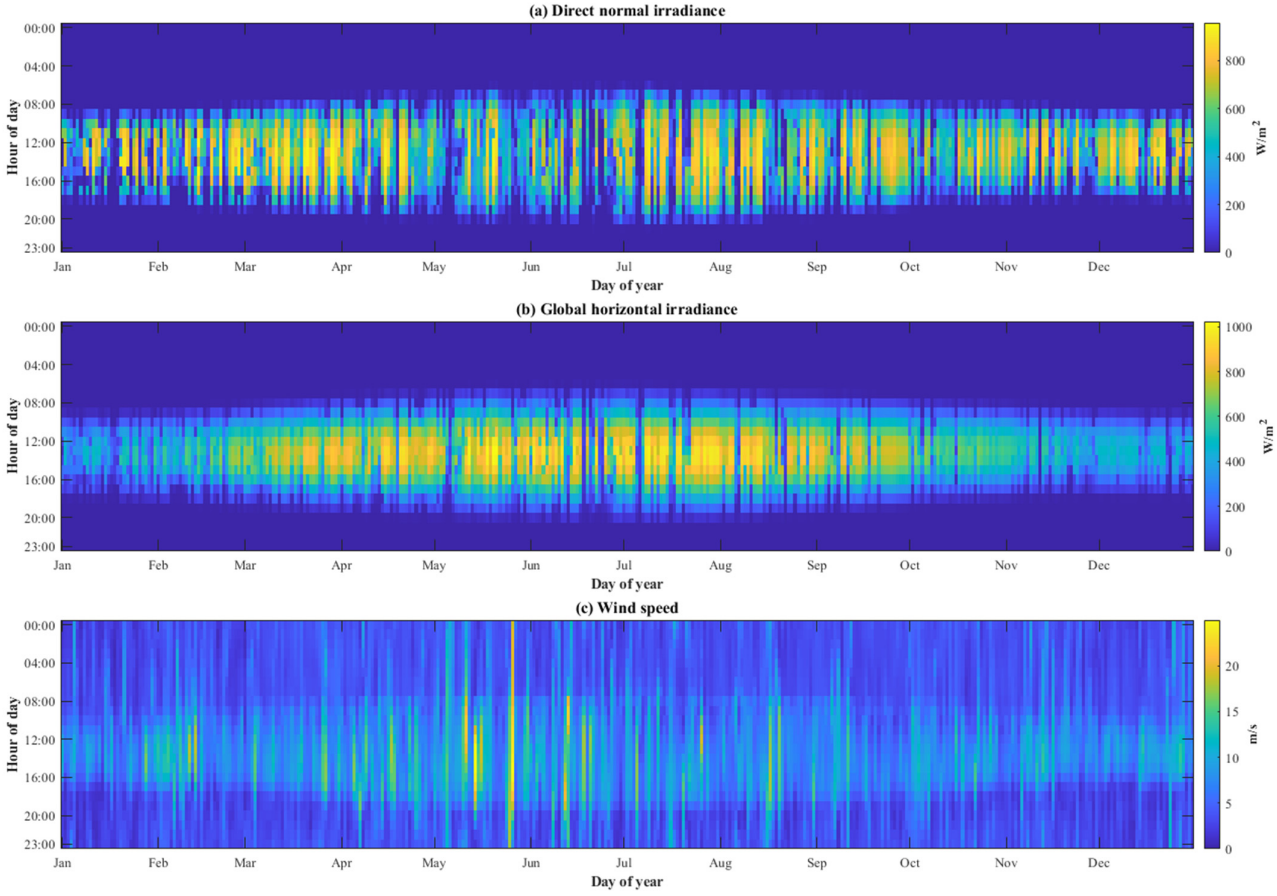


Figure A1. Annual hourly meteorological profiles used in the case study: (**a**) DNI, (**b**) GHI, and (**c**) wind speed.

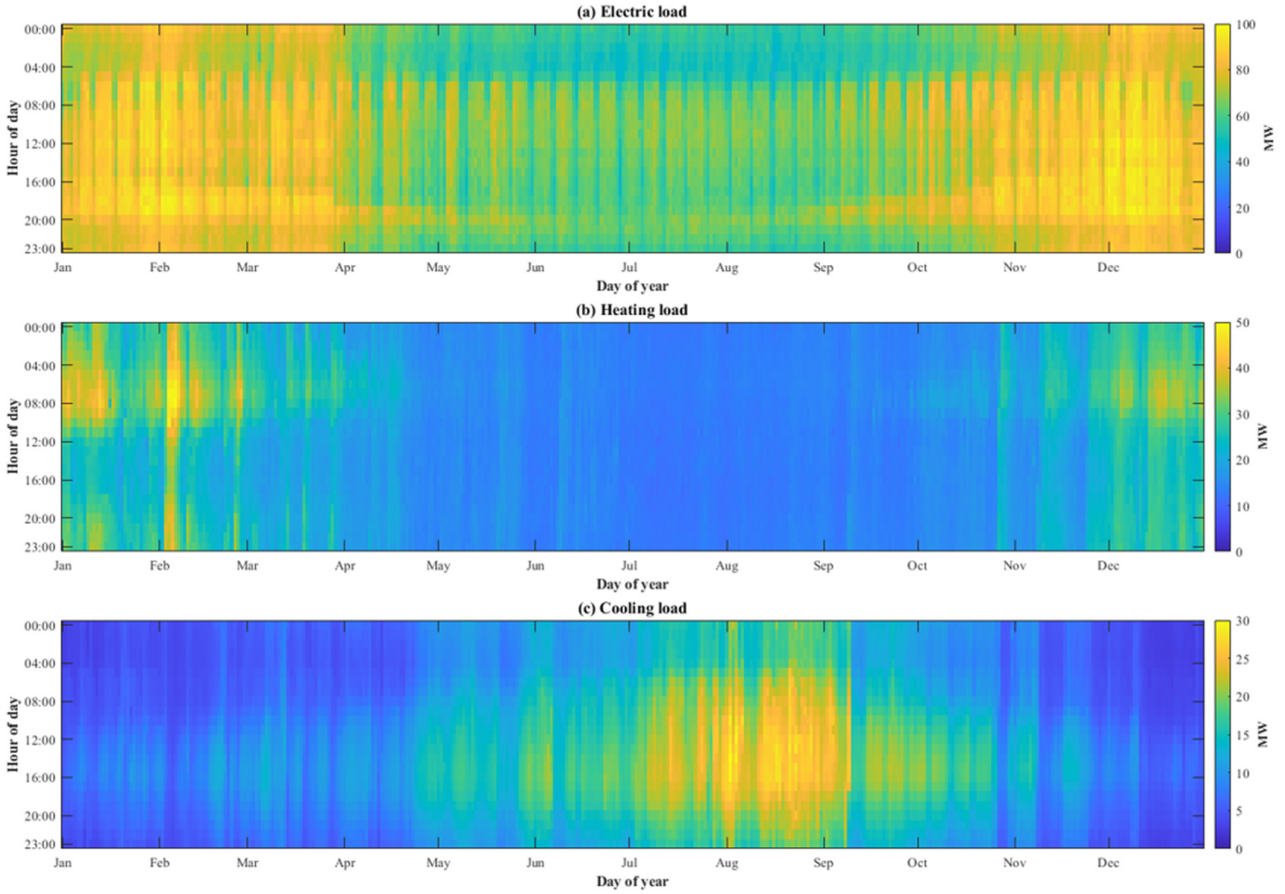


Figure A2. Annual hourly load profiles of the ZCIP: (**a**) electric load, (**b**) heating load, and (**c**) cooling load.

References

1. National Development and Reform Commission. Notice on Advancing the Construction of Zero-Carbon Parks [2025] No. 910. Available online: https://zfxxgk.ndrc.gov.cn/web/iteminfo.jsp?id=20523 (accessed on 15 August 2026).
2. Policy and Economics Research Institute, China Academy of Information and Communications Technology. Research Report on the Pathways and Strategies for Zero-Carbon Park Development. January 2026. Available online: https://www.caict.ac.cn/kxyj/qwfb/ztbg/202601/P020260105557221271888.pdf (accessed on 1 March 2026).
3. National Development Reform Commission; National Energy Administration. Notice on Matters Related to the Orderly Promotion of Direct Green Power Connection Development. Available online: https://www.gov.cn/zhengce/zhengceku/202506/content_7026087.htm (accessed on 10 March 2026).
4. Wu, C.C.; Zhao, Y.H.; Li, W.L.; Fan, J.J.; Xu, H.X.; Yuan, D.K.; Ling, Z.Q. Layered Operation Optimization Methods for Concentrated Solar Power (CSP) Technology and Multi-Energy Flow Coupling Systems. *Energies* **2024**, *17*, 6297. [CrossRef]
5. Wu, C.C.; Zhao, Y.H.; Li, W.L.; Fan, J.J.; Xu, H.X.; Ling, Z.Q.; Yuan, D.K.; Zeng, X.Y. Concentrated Solar Thermal Power Technology and Its Thermal Applications. *Energies* **2025**, *18*, 2120. [CrossRef]
6. Zeng, X.; Xie, H.; Chen, X.; Cao, Q.; Bie, Z. A zero-carbon integrated energy system energized by CSP + PV: A real case of isolated grid. *Sol. Energy* **2025**, *292*, 113440. [CrossRef]
7. Chen, H.; Jia, X.; Wang, H.; Ning, Y.; Li, X.L.; Duanmu, L. Optimization and evaluation of a near-zero carbon energy system: Integration of photovoltaics, heat pumps, and combined thermal and electrical storage solutions. *Energy Convers. Manag.* **2025**, *327*, 119583. [CrossRef]
8. Xie, J.Y.; Chen, X.Y.; Yu, K.; Gan, L.; Hua, H.C.; Wang, B.; Qu, Y.L. Research on the Configuration of a 100% Green Electricity Supplied Zero-Carbon Integrated Energy Station. *Energies* **2024**, *17*, 4111. [CrossRef]
9. Wang, J.J.; Zhou, Y.; Zhang, X.T.; Ma, Z.R.; Gao, Y.F.; Liu, B.X.; Qin, Y.B. Robust multi-objective optimization with life cycle assessment of hybrid solar combined cooling, heating and power system. *Energy Convers. Manag.* **2021**, *232*, 113868. [CrossRef]
10. Han, Z.P.; Han, W.; Ye, Y.Y.; Sui, J. Multi-objective sustainability optimization of a solar-based integrated energy system. *Renew. Sustain. Energy Rev.* **2024**, *202*, 114679. [CrossRef]

11. Shen, H.T.; Zhang, H.L.; Xu, Y.J.; Chen, H.S.; Zhu, Y.L.; Zhang, Z.L.; Li, W.K. Multi-objective capacity configuration optimization of an integrated energy system considering economy and environment with harvest heat. *Energy Convers. Manag.* **2022**, *269*, 116116. [CrossRef]
12. Li, J.Y.; Hua, Z.Y.; Tian, L.; Chen, P.W.; Dong, H. Optimal Capacity Allocation for Life Cycle Multiobjective Integrated Energy Systems Considering Capacity Tariffs and Eco-Indicator 99. *Sustainability* **2024**, *16*, 8930. [CrossRef]
13. Wang, R.; Hasanefendic, S.; Von Hauff, E.; Bossink, B. Towards carbon neutrality: A multi-objective optimization model for photovoltaics systems installation planning. *Sustain. Energy Technol. Assess.* **2024**, *62*, 103625. [CrossRef]
14. Yi, J.H.; Ito, W.; Park, J.K.; Park, H. Impact of carbon emission constraint on design of small scale multi-energy system. *Energy* **2018**, *161*, 792–808. [CrossRef]
15. Barnetche, M.; González-Portillo, L.F.; Abbas, R. Optimum integration of latent heat storage in a solar thermal system for industrial processes: In series or in parallel? *Appl. Therm. Eng.* **2023**, *232*, 121090. [CrossRef]
16. Jiang, J.T.; Liu, L.; Song, J.; Hu, B.; Bi, Y.; Jiang, S.; Dai, Y.J.; Wang, R.Z. Solar-assisted high-temperature heat pumps to achieve off-grid zero-carbon heating in industrial parks. *Renew. Sustain. Energy Rev.* **2026**, *226*, 116412. [CrossRef]
17. Zeng, Q.L.; Tian, Z.Y.; Chen, X.; Li, L.Y.; Ma, L.; Chen, X.Y.; Luo, Y.Q.; Fan, J.H.; Wang, Q. Towards next generation zero carbon heating plants integrated with solar thermal/photovoltaic system and thermal storage. *Energy* **2025**, *336*, 138483. [CrossRef]
18. Wen, Z.; Zhang, X.; Liang, G.; Wang, G.; Wei, X.; Tao, Y.; Wen, F. Cross-sectoral carbon emission flow model based three-stage low-carbon planning framework of integrated electricity-hydrogen-transportation system. *Appl. Energy* **2026**, *423*, 128338. [CrossRef]
19. Luo, H.X.; Zhang, C.; Foo, E.Y.S.; Gooi, H.B.; Sun, L.; Zeng, T.; Chen, T.P. A multi-objective partitioned design method for integrated energy system. *Int. J. Electr. Power Energy Syst.* **2024**, *162*, 110291. [CrossRef]
20. Wu, D.; Han, S.F.; Wang, L.M.; Li, G.Q.; Guo, J.C. Multi-parameter optimization design method for energy system in low-carbon park with integrated hybrid energy storage. *Energy Convers. Manag.* **2023**, *291*, 117265. [CrossRef]
21. Yang, B.J.; Ge, S.Y.; Liu, H.; Zhang, X.H.; Xu, Z.Y.; Wang, S.Y.; Huang, X. Regional integrated energy system reliability and low carbon joint planning considering multiple uncertainties. *Sustain. Energy Grids Netw.* **2023**, *35*, 101123. [CrossRef]
22. Li, X.; Li, T.X.; Liu, L.; Wang, Z.; Li, X.Y.; Huang, J.A.; Huang, J.Q.; Guo, P.F.; Xiong, W. Operation optimization for integrated energy system based on hybrid CSP-CHP considering power-to-gas technology and carbon capture system. *J. Clean. Prod.* **2023**, *391*, 136119. [CrossRef]
23. Guo, X.S.; Lou, S.H.; Wu, Y.W.; Wang, Y.C. Low-carbon Operation of Combined Heat and Power Integrated Plants Based on Solar-assisted Carbon Capture. *J. Mod. Power Syst. Clean Energy* **2022**, *10*, 1138–1151. [CrossRef]
24. Wang, P.Y.; Liu, K.L.; Zhao, J.F.; Zheng, J.Y.; Xu, W.C.; Feng, D.W.; Feng, S.R.; Yang, Y. Low-Carbon Optimal Operation of Multi-Energy Coupled Park Integrated Energy System Considering Carbon Emission Costs. *J. Electr. Eng. Technol.* **2025**, *20*, 4881–4893. [CrossRef]
25. Yin, S.; Chen, S.Y.; Pan, N.; Bu, Y.B.; Lin, C.; Yang, J.W. Optimization of multi-energy collaborative economic operation in plateau zero-carbon parks considering the consumption of wind and solar energy. *J. Renew. Sustain. Energy* **2025**, *17*, 056301. [CrossRef]
26. Zhao, Y.X.; Zhai, R.R.; Liu, S.Y.; Xu, Y.; Liu, L.T. Low carbon economic scheduling of integrated energy system with concentrating solar power and multi-stage hydrogen utilization based on ladder-type carbon trading. *Int. J. Green Energy* **2025**, *22*, 722–739. [CrossRef]
27. Chen, Y.Z.; Xu, Z.C.; Wang, J.; Lund, P.D.; Han, Y.F.; Cheng, T.H. Multi-objective optimization of an integrated energy system against energy, supply-demand matching and exergo-environmental cost over the whole life-cycle. *Energy Convers. Manag.* **2022**, *254*, 115203. [CrossRef]
28. Ye, J.; Shuai, Q.L.; Hua, Q.S. Dynamic programming-based low-carbon and economic scheduling of integrated energy system. *Energy* **2025**, *322*, 135568. [CrossRef]
29. Liu, W. Towards power-to-X and carbon capture technologies for decarbonized green cities: A multi-layer cost-effective energy scheduling approach in integrated energy systems for targeting carbon footprint reduction. *Energy* **2025**, *335*, 137436. [CrossRef]
30. Shao, Y.; Todeschini, G. Optimal dispatch analysis of a multi-energy coupling integrated energy system incorporating salt cavern storage. *Sustain. Energy Technol. Assess.* **2026**, *93*, 105282. [CrossRef]
31. Zhu, H.; Li, J.; Zhu, J.; Huang, D.; Luo, Q.; Liao, C. Distributed optimal power and gas dispatch using variational inequalities and cooperative games. *Appl. Energy* **2026**, *424*, 128412. [CrossRef]
32. Ren, T.; Li, R.; Li, X. Bi-level multi-objective robust optimization for performance improvements in integrated energy system with solar fuel production. *Renew. Energy* **2023**, *219*, 119499. [CrossRef]
33. Li, L.L.; Miao, Y.; Lim, M.K.; Sethanan, K.; Tseng, M.L. Integrated energy system for low-carbon economic operation optimization: Pareto compromise programming and master-slave game. *Renew. Energy* **2024**, *222*, 119946. [CrossRef]
34. Yu, J.Q.; Zhao, J.J.; Zhong, J.J.; Lin, Z.J.; Xu, Y.; Peng, Y.J.; Cai, Y.; Cao, L.H.; Zhang, M.M.; Cao, Y.J. Towards fairness and low-carbon operation of energy hub: A multi-objective optimization framework with energy-carbon bidirectional coupling and heterogeneous uncertainties. *Appl. Energy* **2026**, *409*, 127475. [CrossRef]

35. Duan, Y.; Gao, C.; Xu, Z.H.; Ren, S.Y.; Wu, D.H. Multi-Objective Optimization for the Low-Carbon Operation of Integrated Energy Systems Based on an Improved Genetic Algorithm. *Energies* **2025**, *18*, 2283. [CrossRef]
36. Pan, F.; Zhao, J.M.; Yang, Y.Y.; Feng, H.Y.; Cai, J.H.; Yu, T. Coevolutionary Framework-Based Constrained Multi-Objective Optimization for Optimal Carbon-Energy Combined Flow of a Power Grid. *Math. Probl. Eng.* **2022**, *2022*, 8091485. [CrossRef]
37. Guo, F.Q.; Li, Y.; Xu, Z.; Qin, J.H.; Long, L.M. Multi-objective optimization of multi-energy heating systems based on solar, natural gas, and air- energy. *Sustain. Energy Technol. Assess.* **2021**, *47*, 101394. [CrossRef]
38. Alkuhayli, A.; Dashtdar, M.; Flah, A.; El-Bayeh, C.Z.; Blazek, V.; Prokop, L. Designing a multi-objective energy management system in multiple interconnected water and power microgrids based on the MOPSO algorithm. *Heliyon* **2024**, *10*, e31280. [CrossRef] [PubMed]
39. Li, J.Y.; Gong, Z.Y.; Miao, G.X.; Wang, X.; Yuan, L.; Jia, X.F.; Ma, H. Multi-Objective Optimization of Power-Gas-Heat Integrated Energy System Based on NSGA-II-MOPSO Hybrid Intelligent Algorithm. *J. Electr. Eng. Technol.* **2025**, *20*, 4941–4957. [CrossRef]
40. Cheraghi, R.; Jahangir, M.H. Multi-objective optimization of a hybrid renewable energy system supplying a residential building using NSGA-II and MOPSO algorithms. *Energy Convers. Manag.* **2023**, *294*, 117515. [CrossRef]
41. Chowdhury, S.; Bohre, A.K.; Saha, A.K. Meta-Heuristic Optimization for Hybrid Renewable Energy System in Durgapur: Performance Comparison of GWO, TLBO, and MOPSO. *Sustainability* **2025**, *17*, 6954. [CrossRef]
42. Slama, A.H.; Saidi, L.; Saidi, M.; Benbouzid, M. Metaheuristic Optimization of Hybrid Renewable Energy Systems Under Asymmetric Cost-Reliability Objectives: NSGA-II and MOPSO Approaches. *Symmetry* **2025**, *17*, 1412. [CrossRef]
43. Soheyli, S.; Mayam, M.H.S.; Mehrjoo, M. Modeling a novel CCHP system including solar and wind renewable energy resources and sizing by a CC-MOPSO algorithm. *Appl. Energy* **2016**, *184*, 375–395. [CrossRef]
44. Lv, X.F.; Lv, Y.; Zhu, Y.P. Multi-variable study and MOPSO-based multi-objective optimization of a novel cogeneration plant using biomass fuel and geothermal energy: A complementary hybrid design. *Energy* **2023**, *270*, 126921. [CrossRef]
45. Lin, S.Q.; Ma, T.; Javed, M.S. Prefeasibility study of a distributed photovoltaic system with pumped hydro storage for residential buildings. *Energy Convers. Manag.* **2020**, *222*, 113199. [CrossRef]
46. Blinov, I.V.; Parus, Y.V.; Artemchuk, V.O. Prosumer Operation Planning Model in the Retail Electricity Market. *Tekhnichna Elektrodynamika* **2026**, *2026*, 50–61. [CrossRef]
47. Wang, P.; Hu, B.; Tai, N.; Zhao, L.; Vafai, K. Peak shaving auxiliary service analysis for the photovoltaic and concentrating solar power hybrid system under the planning-dispatch optimization framework. *Energy Convers. Manag.* **2023**, *295*, 117609. [CrossRef]
48. National Development Reform Commission; National Energy Administration. Notice on Matters Relating to the Orderly Promotion of Green Power Direct Connection Development for Multiple Users. Available online: https://www.ndrc.gov.cn/xxgk/zcfb/tz/202605/t20260520_1405313.html (accessed on 15 August 2026).
49. Sengupta, M.; Xie, Y.; Lopez, A.; Habte, A.; Maclaurin, G.; Shelby, J. The National Solar Radiation Data Base (NSRDB). *Renew. Sustain. Energy Rev.* **2018**, *89*, 51–60. [CrossRef]
50. National Laboratory of the Rockies. 2024 Electricity ATB Technologies and Data Overview. Available online: https://atb.nlr.gov/electricity/2024/index#:~:text=The%202024%20Electricity%20Annual%20Technology%20Baseline%20%28ATB%29%20provides,both%20at%20present%20and%20with%20projections%20through%202050 (accessed on 2 August 2026).
51. Vignesh Ramasamy, J.Z.; Woodhouse, M.; O'Shaughnessy, E.; Feldman, D.; Desai, J.; Walker, A.; Margolis, R.; Basore, P. *U.S. Solar Photovoltaic System and Energy Storage Cost Benchmarks, with Minimum Sustainable Price Analysis: Q1 2023*; National Renewable Energy Laboratory (NREL): Golden, CO, USA, 2023. [CrossRef]
52. Energy Data Center. Electricity Price Inquiry. Available online: https://energydc.cn/query/2026-09-07/gansu/industrial-commercial-power/two-part-tariff/voltage-1-to-10kv-20kv (accessed on 1 September 2026).
53. Hu, B.; Cai, F.; Tai, N.; Wang, P. Dual-time scale optimal dispatch of the CSP-PV hybrid power plant considering dynamic operation. *Energy* **2024**, *306*, 132488. [CrossRef]
54. Wang, P.; Hu, B.; Vafai, K. A data-driven stochastic model predictive control framework for optimal operation of CSP-PV hybrid system under grid coordination. *Energy Convers. Manag.* **2026**, *348*, 120653. [CrossRef]

Disclaimer/Publisher's Note: The statements, opinions and data contained in all publications are solely those of the individual author(s) and contributor(s) and not of MDPI and/or the editor(s). MDPI and/or the editor(s) disclaim responsibility for any injury to people or property resulting from any ideas, methods, instructions or products referred to in the content.